

Review

# Molecular Imaging of Brain Tumors and Drug Delivery Using CEST MRI: Promises and Challenges

Jianpan Huang <sup>1,†</sup>, Zilin Chen <sup>1,†</sup>, Se-Weon Park <sup>1,2</sup>, Joseph H. C. Lai <sup>1</sup> and Kannie W. Y. Chan <sup>1,2,3,4,5,\*</sup>

<sup>1</sup> Department of Biomedical Engineering, City University of Hong Kong, Hong Kong, China; jp.huang@cityu.edu.hk (J.H.); zilinchen9-c@my.cityu.edu.hk (Z.C.); swpark3-c@my.cityu.edu.hk (S.-W.P.); josephlai5-c@my.cityu.edu.hk (J.H.C.L.)

<sup>2</sup> Hong Kong Centre for Cerebro-Cardiovascular Health Engineering (COCHE), Hong Kong, China

<sup>3</sup> Russell H. Morgan Department of Radiology and Radiological Science, The Johns Hopkins University School of Medicine, Baltimore, MD 21205, USA

<sup>4</sup> Shenzhen Research Institute, City University of Hong Kong, Shenzhen 518057, China

<sup>5</sup> Tung Biomedical Science Centre, City University of Hong Kong, Hong Kong, China

\* Correspondence: kanniew.y.c@cityu.edu.hk; Tel.: +852-3442-9141

† These authors contributed equally to this work.

**Abstract:** Chemical exchange saturation transfer (CEST) magnetic resonance imaging (MRI) detects molecules in their natural forms in a sensitive and non-invasive manner. This makes it a robust approach to assess brain tumors and related molecular alterations using endogenous molecules, such as proteins/peptides, and drugs approved for clinical use. In this review, we will discuss the promises of CEST MRI in the identification of tumors, tumor grading, detecting molecular alterations related to isocitrate dehydrogenase (IDH) and O-6-methylguanine-DNA methyltransferase (MGMT), assessment of treatment effects, and using multiple contrasts of CEST to develop theranostic approaches for cancer treatments. Promising applications include (i) using the CEST contrast of amide protons of proteins/peptides to detect brain tumors, such as glioblastoma multiforme (GBM) and low-grade gliomas; (ii) using multiple CEST contrasts for tumor stratification, and (iii) evaluation of the efficacy of drug delivery without the need of metallic or radioactive labels. These promising applications have raised enthusiasm, however, the use of CEST MRI is not trivial. CEST contrast depends on the pulse sequences, saturation parameters, methods used to analyze the CEST spectrum (i.e., Z-spectrum), and, importantly, how to interpret changes in CEST contrast and related molecular alterations in the brain. Emerging pulse sequence designs and data analysis approaches, including those assisted with deep learning, have enhanced the capability of CEST MRI in detecting molecules in brain tumors. CEST has become a specific marker for tumor grading and has the potential for prognosis and theranostics in brain tumors. With increasing understanding of the technical aspects and associated molecular alterations detected by CEST MRI, this young field is expected to have wide clinical applications in the near future.



**Citation:** Huang, J.; Chen, Z.; Park, S.-W.; Lai, J.H.C.; Chan, K.W.Y.

Molecular Imaging of Brain Tumors and Drug Delivery Using CEST MRI: Promises and Challenges.

*Pharmaceutics* **2022**, *14*, 451. <https://doi.org/10.3390/pharmaceutics14020451>

Academic Editors: Sangeeta Ray and Ethel J. Ngen

Received: 27 January 2022

Accepted: 17 February 2022

Published: 20 February 2022

**Publisher's Note:** MDPI stays neutral with regard to jurisdictional claims in published maps and institutional affiliations.



**Copyright:** © 2022 by the authors. Licensee MDPI, Basel, Switzerland. This article is an open access article distributed under the terms and conditions of the Creative Commons Attribution (CC BY) license (<https://creativecommons.org/licenses/by/4.0/>).

**Keywords:** CEST; MRI; molecular imaging; brain tumor; contrast agents; chemotherapeutics; drug delivery

## 1. Introduction

Brain tumors are hard to diagnose early and treat. Advances in genomics have enabled the study of molecular alterations in tumors which is critical for the diagnosis and prognosis of brain tumors, as well as to guide treatments. Glioblastoma multiforme (GBM) is the most lethal form of brain tumors. Many related molecular alterations have been found, such as epidermal growth factor receptor (EGFR), isocitrate dehydrogenase (IDH), and O-6-methylguanine-DNA methyltransferase (MGMT) [1]. These alterations do not only vary among different types of brain tumors, the level of alterations is also heterogeneous within tumors. Historically, brain tumor diagnosis is based on histologic features. The inclusion of new multiple assessment parameters could address challenges in brain tumor

diagnosis, treatment planning, and evaluation. Some of these molecular alterations have been incorporated into the diagnostic criteria of brain tumors [2]. For example, IDH mutation is one of the assessment criteria in diffusive gliomas and astrocytoma. MGMT has been found to associate with improved response to treatment with temozolomide (TMZ) and longer overall survival [2]. Imaging is an indispensable way to address the heterogeneity within tumors. Chemical exchange saturation transfer (CEST) is an emerging molecular imaging approach which enables the assessments of molecular alterations in brain tumors [3–45].

CEST MRI was named by Ward and Balaban in 2000 [46]. It detects exchangeable protons of molecules, such as amide protons of proteins/peptides (amide proton transfer, APT at 3.5 ppm) [3,47,48], aliphatic protons of lipids (nuclear Overhauser effect, NOE at −3.5 ppm) [43,44], hydroxyl protons (e.g., glucose at 1–2 ppm), and guanidyl protons (e.g., creatine, at 2 ppm) [49–51]. These exchangeable protons can be detected via the acquisition of a CEST spectrum, i.e., Z-spectrum (Figure 1a,c). CEST is capable of detecting multiple molecules in the brain (Figure 1b,c) such as macromolecules (magnetization transfer contrast, MTC), semi-solids (APT and NOE), and metabolites (e.g., glucose and creatine) simultaneously. Further CEST principles can be found in reviews [49–52]. Magnetic resonance spectroscopy (MRS) is a conventional molecular imaging approach. Its clinical applications have been limited by relatively low sensitivity and low spatial resolution. CEST MRI detects molecules via proton exchange with bulk water (110 M) which is abundant in vivo [47,50]. It has an imaging readout that enables relatively high-resolution detection of the spatial distribution of molecules. Thus, CEST could address the clinical needs in molecular imaging. Notably, MRS detects the distinct chemical environments of molecules while CEST detects exchangeable protons and their exchange environment [53,54]. Nevertheless, detecting molecular alterations and their location is invaluable in assessing brain tumors, especially when more than one molecule is altered in brain tumors in various regions [55–58].

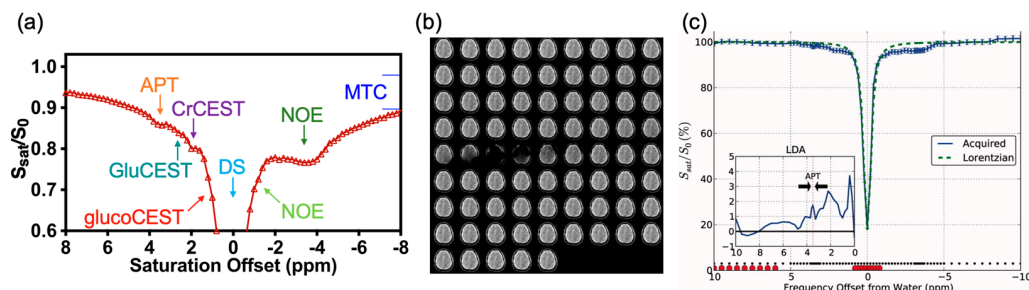


**Figure 1.** (a) Schematic illustration of the Z-spectrum with multiple CEST contrast. APT: amide proton transfer; GluCEST: glutamate CEST; CrCEST: creatine CEST; glucoCEST: glucose CEST; DS: direct water saturation; NOE: nuclear Overhauser effect; MTC: magnetization transfer contrast. (b) Saturated images as a function of saturation frequency for a human brain slice. (c) In vivo Z-spectra and Lorentzian difference analysis (LDA) for a region in the white matter of the human brain. Figure panels (b,c) are reproduced with permission from Jones et al. Magn Reson Med 2012;67(6):1579–1589. Copyright John Wiley and Sons, 2012.

CEST MRI has been applied to grade tumors [5,8,9,19,22,23,27,30–33,39,59–65], assess treatment effects [13,14,21,32,40,66–70], assess progression survival [13,16,17], and evaluate IDH mutation [5,9,17,20,22,24,29,71,72]. Furthermore, the molecular and regional changes in tumors revealed by CEST could inform the development of theranostic approaches for brain tumors, especially for monitoring the changes of multiple components of drug delivery systems longitudinally. This review will focus on the promises of CEST imaging of brain tumors, non-metallic contrast agents, clinical agents and biomaterials for drug delivery, and the challenges of CEST clinical applications.

## 2. CEST Imaging of Brain Tumors

### 2.1. Endogenous Contrast

CEST is capable of detecting the presence of millimolar concentrations of molecules in vivo. The two unique CEST contrasts at 3.5 ppm (APT) and  $-3.5$  ppm (NOE) are widely used to assess brain tumors [5,8,9,13,14,16,17,19–24,27,29–33,39,40,59–72]. Tumors have an acidic microenvironment and CEST is sensitive to pH; hence, CEST could further enhance the detectability of these molecular alterations in tumors [3,58,73]. The principles of CEST and APT imaging have been explained in previous reviews [7,49–52,74–79]. APT and NOE changes could indicate changes in protein/lipid concentration, pH, and cellularity. CEST imaging studies of brain tumors in both animals and humans are summarized in Table 1. With more clinical studies available for GBM and other gliomas [1,2,80], both APT and NOE could provide valuable molecular information for brain tumor assessments, especially towards precise diagnosis and prognosis.

#### 2.1.1. APT-Weighted (APTw) Contrast

CEST contrast at 3.5 ppm could be characterized using the conventional magnetization transfer ratio asymmetry ( $MTR_{asym}$ ) analysis of the Z-spectrum, subtracting signals at 3.5 ppm from  $-3.5$  ppm frequency offsets. There was not much of a magnetization transfer (MT) effect in solutions *in vitro* [47], while an asymmetric MT effect was observed in cross-linked bovine serum albumin (BSA) and semi-solid protein-rich phantoms [81–85]. As demonstrated in early animal studies in 2003, amide proton exchange characterized by  $MTR_{asym}$  (APTw) resulted in hyperintensity in the 9L brain tumor rat model [3,48] which could be ascribed to the elevated cellular proteins and peptides in tumors. Moreover, APTw is robust in the identification of radiation necrosis from tumor recurrence [70,86]. The reduced APTw signal after radiation therapy indicated a molecular tumor response that was detected earlier than other commonly used MRI approaches [70]. APTw CEST was then translated to examine the human brain in 2006 [4].

In human patients, hyperintensities of APTw were found in tumors when compared with the contralateral regions [11,23,25,26,33,36,39,42–44,60,70,87–92] (Table 1). These increased APTw signals were positively correlated to high cellularity [39,70] and were validated by histology. The APTw signal in the core of high-grade tumors was much higher than that of low-grade tumors ( $2.7 \pm 0.3\%$  vs.  $1.2 \pm 0.2\%$ ,  $n = 6$  and 3, respectively), demonstrating a great potential of APTw imaging in tumor grading on a 3 T clinical scanner [60]. Another study of diffuse glioma patients ( $n = 36$ ) [39] also reported a significant correlation between APTw signal and tumor grade. Specifically, APTw signal was  $2.1 \pm 0.4\%$  ( $n = 8$ ),  $3.2 \pm 0.9\%$  ( $n = 10$ ), and  $4.1 \pm 1.0\%$  ( $n = 18$ ) for grade II, III, and IV gliomas, respectively. Moreover, the authors suggested a cutoff APTw value of 2.54% to differentiate high-grade tumors from low-grade tumors with a sensitivity of 93% and specificity of 100%. Similarly, APTw signal increased with tumor grade in diffuse glioma patients ( $n = 46$ ) and an improvement was found by using APTw and apparent diffusion coefficient (ADC) to grade tumors compared to using ADC only (AUC: 0.910 vs. 0.888) [31]. The ability of APTw imaging to identify high- and low-grade gliomas were found to be efficient even using a single representative slice for analysis ( $n = 26$ ) [65]. All these studies demonstrated the great potential of using the APTw signal to grade brain tumors in clinical settings.

#### 2.1.2. NOE Contrast

Brain tumors have a complicated microenvironment and multiple molecules could contribute to the resulting APTw contrast. When we consider CEST at 3.5 ppm and  $-3.5$  ppm independently, the observations are slightly different. CEST at 3.5 ppm alone corrected using the apparent exchange-dependent relaxation (AREX) did not show a significant change in a rat tumor model at 9.4T which was validated by biochemical means [93]. Moreover, the corrected NOE signal showed a significant decrease in the tumor than that in normal tissue [93]. Therefore, it is also valuable to investigate the NOE signal change in tumors. The NOE contrast has a broad range of frequency offsets, from  $-1.5$  to

–5 ppm [33,44,81,94–96]. Most of the studies focused on the offset at around –3.5 ppm as it is more detectable, especially at 3 T [81,97]. NOE at –3.2 to –3.7 ppm, extracted using Lorentzian fitting, showed decreased signals in brain tumors in both animal and human studies [10,33,34,44,90,98–100]. NOE analyzed by AREX showed hypointensity in brain tumors as compared to contralateral regions which correlated to the macromolecular content in tumors [96]. Heo et al. found that the NOE signal showed a negative correlation with tumor grades [33]. This indicates the feasibility of grading brain tumors using NOE imaging. Recently, Zu Z. et al. observed a decrease in NOE signal at –1.6 ppm, which could indicate decreased phospholipids on tumor cell membranes, by restricted phospholipid transfer (RPT) [101]. In general, NOE signals consistently decrease among different analyses in both human and animal studies. Among these studies, there is one study that showed unchanged NOE in a non-enhancing glioma, while APTw signal consistently increased in both enhancing and non-enhancing gliomas [11]. Nevertheless, NOE could be an additional CEST contrast to indicate molecular changes in brain tumors.

## 2.2. Glioblastoma and Gliomas (Grade II, III)

GBM, also known as a grade IV astrocytoma, defined by World Health Organization (WHO), is the most common and aggressive brain tumor. Generally, hyperintensities in APT/APTw images were reported in GBM when compared with contralateral regions [10,11,16,22,25,33,34,36,39,42,60,98]. In human GBM, the increased signals were found to correlate positively to cell proliferation (Ki-67) and cell density, validated by histology [27,39]. The hyperintensity of APTw in tumors was related to high tumor grade and active cell proliferation [39,70,88]. Naturally, hypercellularity leads to an increase in cytosolic protein/peptides in tumor tissues as compared to normal tissues [102,103]. Thus, there is a positive correlation between the APTw signal and cytosolic protein/peptides concentration [90]. However, this might not be held in some tumor regions [90,102,104].

In addition to protein concentration, pH is another factor that attenuates the APT signal via altering the exchange rate. According to previous studies using  $^{31}\text{P}$  NMR spectroscopy, the intracellular pH of GBM is neutral or slightly alkaline with a minor increase of less than 0.1 pH unit [105,106]. On the other hand, a small change of pH may alter the APT signal since the amide proton exchange process is base-catalyzed [90,104,107,108]. The extravascular and extracellular space (EES) of tumors is acidic. A study reported that the contribution of protein concentration and pH change is 66% and 34% in tumors, respectively [108].

The mobility of proteins and peptides is another factor that could contribute to the APTw signal [75]. The liquefactive necrosis and chronic hemorrhage in high-grade brain tumors resulted in an increased APTw signal [45], which was validated by other MRI readouts, such as FLAIR and T1w. The acute hemorrhage showed a higher APTw signal compared to a subacute hemorrhage, while a high APTw signal related to hemorrhage was observed in both tumorous and non-tumorous regions [109]. This hyperintensity of the APTw signal caused by hemorrhage and vascularity was then validated in a rat model [110]. These studies indicated that a high concentration of mobile proteins and peptides in liquid-like necrosis, hemorrhage, and vascularity could also lead to a high APTw signal. Additionally, the viable tumor core had a higher APTw signal than tumor necrosis and normal tissue [45,70]. Therefore, the interpretation of an increase in APTw signal should be cautious and consider the heterogeneity of brain tumors.

Brain tumors are heterogeneous and have different grades. Hence, it is not surprising to observe characteristic regional changes. For example, the APTw changes in dynamic contrast enhancing (DCE) enhancing and non-enhancing tumors could be different [45,111], since there is a higher water content in tumors as compared to normal brain tissues [90]. The enhancing region of high-grade tumors is usually associated with high cell density. Moreover, a decreased ADC value [16,34], intratumoral necrosis [39] and relative cerebral blood volume (CBV) [16] were also observed in GMB. These changes further validated that CEST contrast at 3.5 ppm sensitively detects molecular changes in GBM related to

its aggressiveness. Meanwhile, CEST at 3.5 ppm showed an increased signal in brain tumors with other analyses such as direct saturation-corrected (DISC-CEST) [26,92], three-offset analysis [26], and quasi-steady-state (QUASS) [10]. More neuropathologies could be revealed when combining T1 and diffusion findings in APT interpretation.

GBM has the highest APTw signal among astrocytomas at different grades, including anaplastic astrocytoma at WHO grade III and astrocytoma at grade II [22,39,42,60], indicating CEST contrast could assist in astrocytoma grading. IDH mutation is mainly found in grade II/III gliomas and secondary GBM [112,113]. IDH gene-encoded enzymes participate in several cellular functions, such as amino acid metabolism, lipid metabolism, and genome-wide DNA methylation. IDH mutation and the MGMT promoter methylation have been included as critical prognostic molecular markers for glioma [114]. CEST at 3.5 ppm demonstrated hyperintensity in IDH-wild type when compared with IDH-mutant glioma patients, along with a high level of relative CBV [16,22,29], while showed no significant differences regarding the MGMT promoter methylation status [22]. NOE imaging related to this mutation is quite diverse [5,22]. Overall, CEST at 3.5 ppm may serve as the IDH mutation marker and help in glioma status prediction.

**Table 1.** CEST MRI of brain tumors using endogenous contrast.

Species	Tumor Type (Grade)	B <sub>0</sub> (T)	Analysis Method	CEST Contrast	Molecular/Cellular Changes	Ref.
Rat	Glioma, C6	3	DISC-CEST	APT	Cellular and nuclear atypia	Wu Y. et al., 2019 [92]
Rat	Gliosarcoma, 9L	4.7	MTR <sub>asym</sub>	APTw	Cellular proteins and peptides	Zhou Z. et al., 2003 [3]
Rat	Gliosarcoma, 9L	4.7	MTR <sub>asym</sub>	APTw	pH	Zhou Z. et al., 2003 [48]
Rat	Gliosarcoma, 9L SF188/V + glioma	4.7	MTR <sub>asym</sub>	APTw	Treatment effects (radiation therapy), radiation necrosis, mobile cytosolic proteins, and peptides	Zhou J. et al., 2011 [70]
Rat	Gliosarcoma, 9L	4.7	MTR <sub>asym</sub>	APTw NOE (-2.5 to -5 ppm)	Mobile proteins, peptides, lipids, and metabolites	Zhou J. et al., 2013 [43]
Rat	U87	4.7	MTR <sub>asym</sub>	APTw	Treatment effects (radiation therapy), radiation necrosis, cellularity, nuclear atypia, and vacuolation	Hong X. et al., 2014 [69]
Rat	GBM	4.7	EMR	APT, NOE	Mobile proteins and peptides	Heo HY. et al., 2016 [87]
Rat	GBM	4.7	MTR <sub>REX</sub> , AREX, CESTR, CESTR <sup>nr</sup>	APT, 2 ppm	APT: mobile proteins and peptides, 2 ppm: protein and peptide side-chain amide protons and various amine-related protons	Heo HY. et al., 2017 [89]
Rat	U87	4.7	MTR <sub>asym</sub> EMR	APTw APT, NOE	Amide proton mobile amide proton content or the increased amide proton exchange rate	Lee DH. et al., 2017 [90]
Rat	Glioma	4.7	DISC-CEST	APT NOE	APT: intracellular mobile proteins/peptides concentration NOE: aliphatic and olefinic protons	Zhou IY. et al., 2017 [26]
Rat	Gliosarcoma, 9L	4.7	MTR <sub>asym</sub> EMR	APTw APT, NOE	NA	Heo H. et al., 2019 [91]
Rat	Gliosarcoma, 9L	9.4	AREX	APT, NOE	Protein contents	Xu J. et al., 2014 [93]
Rat	Gliosarcoma, 9L	9.4	Lorentzian	APT (3.6 ppm) NOE (-3.2 ppm) 2 ppm	Amide proton Tumor progression and creatine	Cai K. et al., 2015 [115]
Rat	Gliosarcoma, 9L; glioma, F98	9.4	Lorentzian	2 ppm	Creatine and tumor aggressiveness	Cai K. et al., 2017 [116]
Rat	Gliosarcoma, 9L	9.4	MTR <sub>asym</sub> / AREX	3 ppm	Amine and protein	Zhang XY. et al., 2017 [117]
Rat	ENU1564 (brain metastasis model)	9.4	APTR*	APT	Protein concentration and pH	Ray KJ. et al., 2019 [107]
Rat	Gliosarcoma, 9L	9.4	Lorentzian	3 ppm	Glutamate	Debnath A. et al., 2020 [118]
Rat	Gliosarcoma, 9L	9.4	RPT	NOE (-1.6 ppm)	Phospholipids on cell membranes	Zu Z. et al., 2020 [101]

**Table 1.** Cont.

Species	Tumor Type (Grade)	B <sub>0</sub> (T)	Analysis Method	CEST Contrast	Molecular/Cellular Changes	Ref.
Mouse	GBM, patient cells	7	MTR <sub>asym</sub>	APTw	Proliferation, cellular acidification, and treatment effect (TMZ)	Sagiyama K. et al., 2014 [40]
Mouse	Glioma, GL261	7	MTR <sub>asym</sub>	3 ppm	Amine, pH, cellularity, and necrosis	Harris RJ. et al., 2015 [38]
Mouse	U87MG	9.4	AACID	AACID (amide at 3.5 ppm, amine at 2.75 ppm)	Intracellular pH and treatment effect	Albatany M. et al., 2019 [66]
Human (n = 10)	GBM (IV), oligodendrogloma (III), LGO (II), LGA (II), Meningioma	3	MTR <sub>asym</sub>	APTw	Cellular protein/peptide and intracellular pH	Jones CK. et al., 2006 [4]
Human (n = 9)	GMB (IV), AO (III), AA (III), LGO (II), LGA (II)	3	MTR <sub>asym</sub>	APTw	Glioma grading, cytosolic protein and peptide, and intracellular pH	Zhou J. et al., 2008 [60]
Human (n = 12)	GBM (IV), astrocytoma (III), oligodendrogloma (III)	3	MTR <sub>asym</sub>	APTw	Viable tumor core, edema, necrosis, mobile protein, and peptide	Wen Z. et al., 2010 [45]
Human (n = 14)	GBM (IV), AA (III), LGO (II), LGA (II), LGOA (II)	3	MTR <sub>asym</sub>	APTw	Protein content	Zhou J. et al., 2013 [42]
Human (n = 36)	GBM (IV), AO (III), AA (III), AOA (III), LGA (II), LGO (II), LGOA (II)	3	MTR <sub>asym</sub>	APTw	Glioma grading, necrosis, cell density, and proliferation	Togao O. et al., 2014 [39]
Human (n = 25)	Glioma (II–IV)	3	MTR <sub>asym</sub>	3 ppm	An acidic signature, treatment effect (CRT), and PFS	Harris RJ. et al., 2015 [38]
Human (n = 26)	GBM (IV), AA (III), AO (III), LGO (II), LGOA (II)	3	MTR <sub>asym</sub>	APTw	Glioma grading	Sakata A. et al., 2015 [65]
Human (n = 13)	GBM (IV), Gliomas (low-grade), meningiomas, lymphoma	3	MTR <sub>asym</sub>	APTw	NA	Togao O. et al., 2015 [36]
Human (n = 11)	High-grade glioma	3	EMR	APT, NOE	NA	Heo HY. et al., 2016 [119]
Human (n = 32)	High-grade glioma Lymphomas	3	MTR <sub>asym</sub>	APTw	Differentiate lymphomas from high-grade glioma and protein	Jiang S. et al., 2016 [64]
Human (n = 65)	Glioma (II–IV)	3	MTR <sub>asym</sub>	APTw	Proliferation	Park J. et al., 2016 [32]
Human (n = 32)	GBM (IV), AA (III), gliomas (low-grade)	3	MTR <sub>asym</sub>	APTw	Cellularity	Ma B. et al., 2016 [68]
Human (n = 65)	Glioma (II–IV)	3	MTR <sub>asym</sub>	APTw	Proliferation	Park J. et al., 2016 [32]
Human (n = 32)	GBM (IV), AA (III), gliomas (low-grade)	3	MTR <sub>asym</sub>	APTw	Cellularity	Ma B. et al., 2016 [68]
Human (n = 7)	AA (III), LGO (II), LGA (II)	3	MTR <sub>asym</sub>	APTw	NA	Zhang Y. et al., 2016 [88]
Human (n = 44)	Glioma (II–IV)	3	MTR <sub>asym</sub>	APTw	Glioma grading and proliferation	Bai Y. et al., 2017 [63]
Human (n = 46)	Glioma (II–IV)	3	MTR <sub>asym</sub>	APTw	Glioma grading, protein, and peptide	Choi YS. et al., 2017 [31]
Human (n = 24)	Glioma (II–IV), edema	3	MTR <sub>asym</sub>	APTw	Cellularity, proliferation, and glioma grading	Jiang S. et al., 2017 [30]
Human (n = 27)	Glioma (II)	3	MTR <sub>asym</sub>	APTw	IDH mutation	Jiang S. et al., 2017 [29]
Human (n = 42)	Glioma (II–IV)	3	MTR <sub>asym</sub>	APTw	Glioma grading, proliferation, choline, and N-acetylaspartate	Su C. et al., 2017 [27]
Human (n = 18)	GBM (IV)	3	MTR <sub>asym</sub>	APTw	MGMT promoter methylation status	Jiang S. et al., 2018 [24]
Human (n = 57)	Meningioma	3	MTR <sub>asym</sub>	APTw	Intracellular proteins and peptides	Joo B. et al., 2018 [23]
Human (n = 42)	Glioma (II–IV)	3	MTR <sub>asym</sub>	APTw	MGMT prediction	Su L. et al., 2018 [20]
Human (n = 21)	GBM (IV), glioma (II), metastases, meningioma, chronic infarction	3	MTR <sub>asym</sub>	APTw	Proteins and peptides	Sun H. et al., 2018 [120]
Human (n = 32)	Glioma (II–IV)	3	Z-spectral fitted, MTR <sub>asym</sub>	APT APTw	Glioma grading and proliferation	Zhang J. et al., 2018 [19]
Human (n = 51)	Glioma (II–IV)	3	MTR <sub>asym</sub>	APTw	Glioma grading and mobile cellular proteins	Zou T. et al., 2018 [62]
Human (n = 21)	GBM (IV), gliosarcoma (IV), AA (III),	3	MTR <sub>asym</sub>	APTw	Cellularity, proliferation, tumor recurrence, and a marker for active glioma	Jiang S. et al., 2019 [18]

**Table 1.** Cont.

Species	Tumor Type (Grade)	B <sub>0</sub> (T)	Analysis Method	CEST Contrast	Molecular/Cellular Changes	Ref.
Human (n = 71)	Glioma (III and IV)	3	MTR <sub>asym</sub>	APTw	Overall survival, PFS, and IDH mutation	Joo B. et al., 2019 [17]
Human (n = 14)	GBM (IV)	3	MTR <sub>asym</sub> Lorentzian	APTw APT	IDH and pH	Schure JR. et al., 2019 [108]
Human (n = 90)	Glioma (II–IV)	3	MTR <sub>asym</sub>	3 ppm	Cerebral blood volume and IDH mutation	Wang YL. et al., 2019 [72]
Human (n = 26)	Glioma (II, IV) Metastasis	3	MTR <sub>asym</sub>	APTw (3.5±0.4 ppm)	Glioma grading, MGMT, and IDH	Durmou F. et al., 2020 [61]
Human (n = 59)	Glioma (II, III)	3	MTR <sub>asym</sub> , machine learning	APTw	IDH1 mutation	Han Y. et al., 2020 [71]
Human (n = 54)	GBM (IV)	3	MTR <sub>asym</sub>	APTw	Treatment effect (bevacizumab), 12-month progression, PFS, and CBV	Park J. et al., 2020 [13]
Human (n = 30)	Glioma (III, IV)	3	MTR <sub>asym</sub>	APTw	Treatment effect (radiotherapy or CRT), tumor recurrence, and protein	Liu J. et al., 2020 [14]
Human (n = 46)	Glioma (II–IV)	3	MTR <sub>asym</sub>	APTw	Cellularity and CBV glioma grading	Schon S. et al., 2020 [59]
Human (n = 18)	GBM (IV), AA (III), astrocytoma (III), LGO (II), LGA (II)	3	MTR <sub>asym</sub> Lorentzian	APTw APT	Cytosolic protein content, mobile proteins, and semisolid macromolecules	Warnert EAH. et al., 2021 [11]
Human (n = 51)	Glioma (II–IV)	3	MTR <sub>asym</sub>	APTw	Glioma grading (peptide or protein concentrations), cellularity, proliferation, and IDH mutation	Xu Z. et al., 2021 [9]
Human (n = 48)	Glioma (II–IV), Brain metastases	3	MTR <sub>asym</sub> , machine learning	APTw	Protein content	Sartoretti E. et al., 2021 [12]
Human (n = 19)	GBM, meningioma, brain metastasis	3	QUASS	APTw, MT&NOE (−1.5 ppm)	−1.5 ppm: proliferation	Wu Y. et al., 2021 [10]
Human (n = 48)	High-grade glioma (III,IV) Low-grade glioma (I,II)	3	CESTR <sup>nr</sup> , EMR	APT	Glioma grading (proteins and peptides)	Zhang H. et al., 2021 [8]
Human (n = 81)	H3K27M-mutant associated brainstem glioma	3	MTR <sub>asym</sub>	APTw	H3K27M mutation, proliferation, pH, and protein and peptide metabolism	Zhuo Z. et al., 2021 [6]
Human (n = 113)	Glioma (II–IV)	3	Lorentzian	APT 2 ppm	Glioma grading (cellularity, mobile protein, and peptides), and IDH mutation Creatine and 1p/19q co-deletion	Su C. et al., 2022 [5]
Human (n = 1)	AA (III)	7	MTR <sub>asym</sub> Lorentzian	−3.5 ppm APT (3.3 to 3.7 ppm) NOE (−2 to −5 ppm)	Cellular density	Jones CK. et al., 2013 [44]
Human (n = 2)	GBM (IV), glioma (II or III)	7	MTR <sub>asym</sub>	−3 ppm	Necrosis and the structural integrity of proteins in cells (protein folding)	Zaiss M. et al., 2013 [121]
Human (n = 12)	GBM (IV)	7	MTR <sub>asym</sub>	3.3 ppm	Protein structures proliferation	Paech D. et al., 2014 [41]
Human (n = 15)	GBM (IV)	7	MTR <sub>asym</sub>	3.3 ppm	Cell density and edema	Paech D. et al., 2015 [37]
Human (n = 1)	LGO (II)	7	AREX	APT, NOE	NA	Windschuh J. et al., 2015 [35]
Human (n = 10)	GBM (IV)	7	AREX	3.5 ppm, NOE	Protein and lipid	Zaiss M. et al., 2015 [34]
Human (n = 10)	Gliomas (II–IV)	7	MTR <sub>asym</sub> EMR	APTw APT (3.3 to 3.7 ppm) NOE (−3.3 to −3.7 ppm)	Glioma grading	Heo HY. et al., 2016 [33]
Human (n = 11)	GBM (IV)	7	MTR <sub>asym</sub> , dnsAREX	3.5 ppm	Amide proton and pH	Zaiss M. et al., 2017 [25]
Human (n = 31)	Glioma (II–IV)	7	MTR <sub>asym</sub> , dnsAREX	APT (3.5 ppm)	Glioma grading, IDH mutation, and MGMT promoter methylation status	Paech D. et al., 2018 [22]
Human (n = 20)	GBM (IV)	7	Lorentzian MTR <sub>asym</sub> dnsAREX	NOE APT APT	Treatment effect (First-line therapy)	Regnery S. et al., 2018 [21]
Human (n = 12)	GBM (IV), LGO (II), LGA (II)	7	AREX dnsAREX	NOE APT	Treatment effect (CRT)	Meissner JE. et al., 2019 [67]
Human (n = 26)	GBM (IV), AA (III)	7	AREX, dnsAREX	APT	Overall survival and PFS, amino acid, and protein	Paech D. et al., 2019 [16]

**Table 1.** Cont.

Species	Tumor Type (Grade)	B <sub>0</sub> (T)	Analysis Method	CEST Contrast	Molecular/Cellular Changes	Ref.
Human (n = 1)	GBM	9.4	Lorentzian	3.5 ppm, NOE (−1.6, −3.5 ppm), 2 ppm, 2.7 ppm	Proteins and lipids	Zaiss M. et al., 2018 [98]

B<sub>0</sub>, static magnetic field; GBM, glioblastoma; AO, anaplastic oligodendrogloma; AA, anaplastic astrocytoma; AOA, anaplastic oligoastrocytoma; LGO, low-grade oligodendrogloma; LGA, low-grade astrocytoma; LGOA, low-grade oligoastrocytoma; TMZ, temozolomide; CRT, chemoradiotherapy; PFS, progression-free survival; Cho/NAA, choline-to-n-acetyl-aspartate; I-IV: WHO classification tumor grade I-IV; CBV, cerebral blood volume; DISC, direct saturation-corrected; QUASS, quasi-steady-state. APTw refers to MTR<sub>asym</sub> at 3.5 ppm, APT refers to CEST at 3.5 ppm, NOE refers to CEST at −3.5 ppm, unless the offset is specifically indicated.

### 2.3. Multiple CEST Contrast in Brain Tumors

Multiple CEST contrast could be beneficial for assessing the heterogenous molecular alterations in brain tumors. Other than the most studied CEST signals at 3.5 ppm and −3.5 ppm, other frequency offsets could provide valuable information within tumors, e.g., CEST contrast at 2 ppm was found to correlate with tumor aggressiveness [115,116]. An increased amine contrast at 2–3 ppm was observed in both animal [43,117] and human studies [38]. This could indicate the acidic microenvironment and an increase of amino acids in tumors which had low perfusion and a high level of hypoxia validated by cerebral blood flow (CBF) [38]. An increase of CEST contrast at 3 ppm could correspond to the increases in glutamate, glycine, and phenylalanine in tumors compared with contralateral regions [118]. These CEST contrasts could correlate with pH changes in tumors [38]. Amine/amide concentration independent detection (AACID) calculated based on an amide signal at 3.5 ppm and an amine signal at 2.75 ppm indicated the intracellular pH changes in mice at 9.4 T [66]. A recently published study including 113 brain tumor patients revealed changes in these multiple contrasts, including direct water saturation (DS), MTC, APT, NOE, and CEST at 2 ppm, reflected different tumor status and provided improved sensitivity and specificity in tumor diagnosis [5].

Moreover, multiple CEST contrast is reported to be sensitive to the treatment response. CEST at 3.5 ppm after anti-angiogenic therapy, radiation therapy, or chemoradiotherapy was decreased [13,14,21,32,40,66–70], but remained high in the case of tumor recurrence in rodents [70,92]. In patients, using more than one CEST contrast (e.g., APT and NOE) could identify the responders [21,67]. CEST at 3.5 ppm signal was reported to be well correlated with overall survival and progression-free survival [13,16,17], while CEST at −3.5 ppm signal was well correlated with overall survival [16]. In general, a change in CEST at 3.5 ppm and −3.5 ppm signal could be predictive for treatment responses and survival.

In summary, APTw contrast is unique in grading brain tumors at 3 T [27,30,39,60,64,65], although it could have multiple origins. It can be applied to study alterations in proteins, peptides, cellularity, proliferation, necrosis, IDH and MGMT, and metabolites. In addition to APT and NOE, other CEST contrasts have been explored to further study the underlying molecular alterations, including the regional alterations, in brain tumors, especially with the aid of radiomics [6,12].

### 3. Non-Metallic CEST Contrast Agents for Brain Tumor Imaging

While endogenous CEST contrast demonstrated uniqueness in imaging brain tumors, other non-metallic CEST contrast agents have been exploited to further enhance the contrast of specific molecular alterations in tumors [50,78,122–125]. Compared to endogenous molecules, the administration of contrast agents could provide a relatively high local concentration. Some contrast agents generate contrast further away from endogenous contrast, which typically exchanges at 1–4 ppm, could enhance the sensitivity by minimizing overlaps with background signals. The current clinical approach for brain tumor detection using MRI mainly relies on the use of gadolinium-based contrast agents (GBCAs) which do not enhance all types of tumors; in particular, the non-enhanced tumors could be malignant [126]. Moreover, it has safety concerns related to the development of incurable

nephrogenic systematic fibrosis in renal compromised patients [127]. The Food and Drug Administration (FDA) also announced gadolinium retention in the brain could last for years [128,129].

One of the widely studied non-metallic CEST contrast agents for brain tumor imaging is D-glucose [123]. Glucose ( $C_6H_{12}O_6$ ) is a hexose with five hydroxyl (-OH) protons which can be detected by CEST MRI (Figure 2). In 2012, glucose was studied as a safe biocompatible nonmetallic contrast agent of CEST MRI [130–134] (Figure 2). Its hydroxyl protons generated CEST contrast at 0.8–2.2 ppm at 11.7 T (glucoCEST) [130,135]. In the first studies, researchers demonstrated that glucoCEST can be used to identify breast tumors and colon tumors in mouse models [130,135]. In breast tumors, glucoCEST is the only imaging modality in this study that could identify aggressive MDA-MB-231 tumors from less aggressive MCF-7 tumors, while conventional DCE-MRI using GBCAs and fluorodeoxyglucose (FDG) positron emission tomography (PET) did not show much difference. In the colon tumor study, researchers observed complementary signal changes in glucoCEST compared to FDG-PET. Regarding the uniqueness of breast tumor identification, the three-compartment model is proposed to explain the contributions to the signal changes (Figure 2a). D-glucose will participate in the three compartments, i.e., vasculature (v), EES, and intracellular space, while FDG is mainly distributed intracellularly. Once D-glucose goes intracellular, it is metabolized to lactate swiftly, as such, the detection of D-glucose in the EES of a tumor with low pH (~6.8 pH) could be more robust [130]. This was further illustrated in a brain glioblastoma mouse model (U87EGFRVIII) with inhibited hexokinase activity in which more glucoCEST contrast was detected in tumors with inhibition [136]. This could further support the major contributions from (v) and EES in tumors. Dynamic imaging of glucose was used in this study, i.e., dynamic glucose-enhanced (DGE) MRI [137–140]. DGE revealed a blood-brain-barrier (BBB) breakdown and an increased blood volume in brain tumors [139] (Figure 2b). It was translated to image brain tumor patients in 2015 [140] (Figure 2c), and can be applied to detect the BBB breakdown in patients at 3 T [141,142].

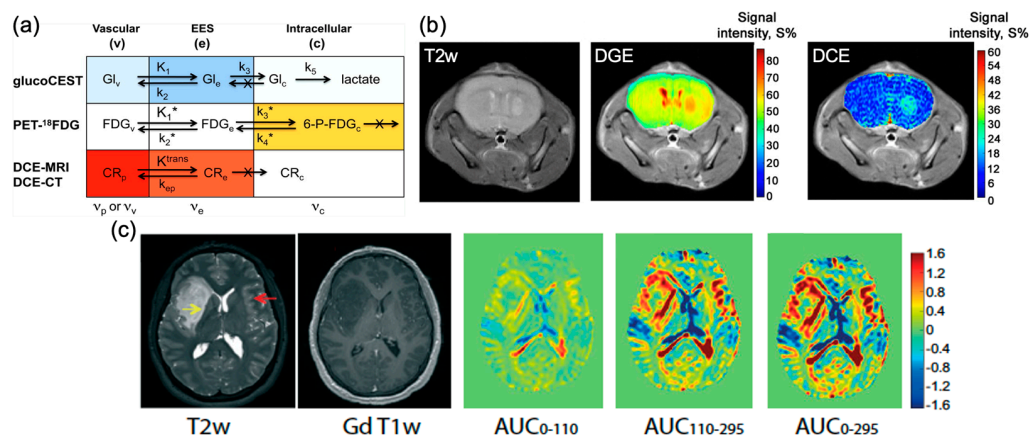


**Figure 2.** GlucoCEST and DGE MRI in brain tumors. (a) An overview of rate constants and contrast contributions (darker color = higher contrast; white is negligible contrast) for glucoCEST, <sup>18</sup>FDG-PET, and contrast-enhanced MRI and CT in tumors. (b) T2-weighted image, DGE image at 300 s, and DCE image at 300 s for a mouse brain with tumor. (c) T2-weighted, gadolinium-T1-weighted, and DGE-based AUC images for different time periods (0–110 s, 110–295 s, 0–295 s) relative to the start of infusion for a human brain with glioma. Reproduced with permission from [130], John Wiley and Sons, 2012 [139], John Wiley and Sons, 2015 [140], MDPI, 2015.

Other sugar analogs, such as 2-deoxy-D-glucose (2-DG) [143,144] and 3-O-Methyl-D-Glucose (3-OMG) [133,145], have been studied to image brain tumors in rodents. Notably, both 2-DG and 3-OMG cannot be metabolized, thus they mainly stay intracellularly. This could be similar to the distribution of FDG in PET imaging, which the tracer trapped intra-

cellularly. Hence, this provides a wide imaging window for the intracellular compartment. Poly-L-glutamate could also enhance brain tumor imaging via generating CEST contrast at 3 ppm upon enzymatic cleavage in rat brain tumors [146]. Thus, many compounds could be repurposed as CEST contrast agents for brain tumor imaging.

#### 4. Imaging Drugs and Drug Delivery

##### 4.1. Imaging Drugs and Drug Delivery Using CEST MRI

Many chemotherapeutics can be detected by CEST MRI. Liu et al. have shown that anticancer drugs, such as gemcitabine and their analogs, generated CEST contrast at 2–3 ppm in the presence of -OH and -NH<sub>2</sub> exchangeable protons [147] (Figure 3a–d). Deoxycytidine was phosphorylated by deoxycytidine kinase in cells, thus imaging deoxycytidine could indicate this enzymatic activity [84]. Melphalan with -NH<sub>2</sub> exchangeable protons is another potential drug candidate for brain tumor treatment that can be detected by CEST at 2.5 ppm [147].

Imaging drug delivery has implications in the design of drug carriers and detection of the amount of drugs delivered to tumors, thereby assessing the therapeutic effects. Liposomes are versatile carriers for both contrast agents and drugs. They were approved as a carrier for doxorubicin, a chemotherapeutic in 1995 [148], and the generic version was approved in 2013. Doxil reaches tumors based on the enhanced permeability and retention (EPR) effect to passively target tumors. Liposomes have been used as carriers for non-metallic CEST contrast agents [51,122,124,149–152]. Liposomes containing barbituric acid (BA) CEST contrast agents could target tumors based on EPR [153–155] (Figure 3e), and reveal the therapeutic effect of tumor necrosis factor-alpha (TNF- $\alpha$ ) (Figure 3f), which induce hyperpermeability in vasculature and destruction of the vascular lining [153]. However, the presence of the BBB could limit the delivery of drug-containing liposomes to brain tumors. In the considerations of the presence of the BBB and the efficacy of drugs under physiological environment, we recently developed a CEST MRI-guided nose-to-brain drug delivery system based on CEST detectable liposomes [156]. The benefit of intranasal drug delivery is that it can bypass the BBB and hence enables relatively high dose of drugs reaching the brain. There are two clinical trials underway for intranasal delivery of chemotherapeutics to the GBM (NCT04091503; NCT02704858).

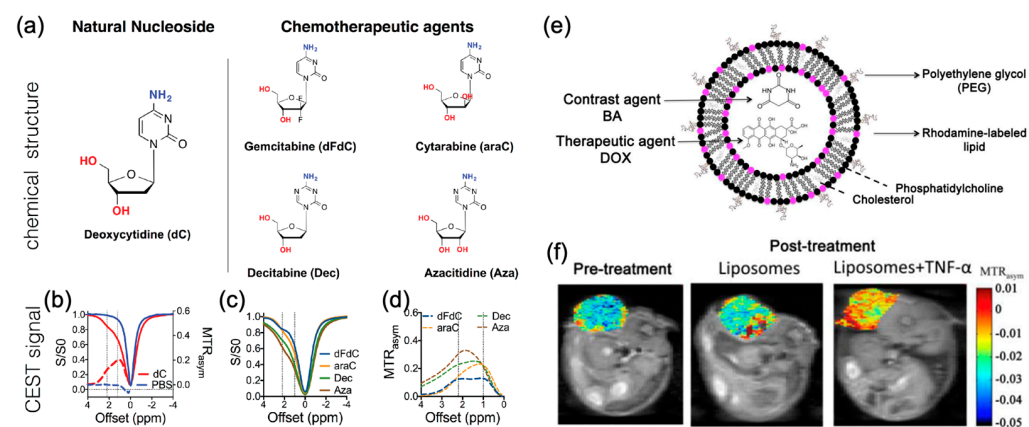


**Figure 3.** Contrast agent/drug-loaded liposome for CEST imaging. (a) The chemical structure of cytidine-based agents and (b–d) their CEST MRI contrast, as shown both by z-spectra (b,c) and MTR<sub>asym</sub> plots (b,d). (e) Cartoon depicting the contrast agent/therapeutic agent (BA/DOX) co-loaded liposome. (f) MTR<sub>asym</sub> maps at 5 ppm for a mouse bearing CT26 subcutaneous tumors before and after treatment with BA/DOX co-loaded liposome. Reproduced with permission from [147], Impact Journals, 2016 [153], Elsevier, 2014.

#### 4.2. Theranostic Applications

To further extend the benefit of CEST in detecting molecules/drugs with their natural labels to theranostic applications, Yuan et al. designed cell-penetrating and self-assembling olsalazine nanoparticles. Olsalazine is a chemotherapeutic agent having hydroxyl protons that exchange at 9.8 ppm. The molecular structure and sequence of reactions are shown in Figure 4a [157]. In brief, in the presence of glutathione (GSH) and furin, the olsalazine (Olsa)-RVRR will form self-assembled particles in cells. In mice bearing both high and low furin expressing tumors, the tumor with high furin expression had a significantly higher CEST contrast at 9.8 ppm compared to the tumor with low furin expression (Figure 4b) [157]. CEST contrast at 9.8 ppm is unique for Olsalazine and did not overlap with endogenous CEST contrast. The increase in this CEST contrast over time indicates the accumulation of these drug nanoparticles in tumors.

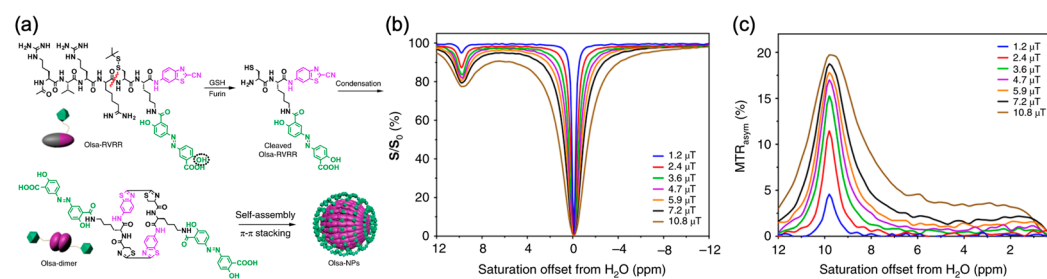


**Figure 4.** (a) Schematic illustration for the formation of Olsa-NPs by furin-mediated intracellular reduction and condensation of Olsa-RVRR; (b) Z-spectra and (c) MTR<sub>asym</sub> values of 10 mM olsalazine for different saturation powers. Olsa: olsalazine; NPs: nanoparticles. Reproduced with permission from [157], Springer Nature, 2019.

Other than nanoparticles, a hydrogel is another potential biomaterial for drug delivery to brain tumors. The CEST imaging of a hydrogel incorporated with liposomes as a pH-nanosensor indicated the potential to detect small and local changes in pH for detecting cell viability *in vivo* [158]. Pemetrexed (Pem), which is an anticancer drug with -NH<sub>2</sub> (heterocyclic ring amide), conjugated with glutamic acid and phenylalanine and formed a nanofiber hydrogel that generates CEST contrast at 5.2 ppm in a mouse brain via local injection (Figure 5) [159]. The current adjuvant treatment after brain tumor resection is to place a carmustine wafer at the tumor resection site [160,161]. Its wide clinical application has been hindered by the side effect of wafer degradation. Studies have demonstrated the potential of using a hydrogel instead of the wafer for local drug delivery to brain tumor resection sites [162–164]; such a hydrogel loaded with paclitaxel showed a controlled and sustainable release of the drug over 6 weeks after injection in the proximity of the GBM in mice [162,165]. In another hydrogel study, Han et al. showed that an injectable liposomal hydrogel generated CEST contrast at both 5 ppm and -3.4 ppm, which indicate the intraliposomal drug barbituric acid (BA) and liposomes, respectively. This is the first use of CEST contrast at -3.4 ppm for liposome imaging at 3 T [166]. Interestingly, the release at 5 ppm is relatively faster than that at -3.4 ppm, indicating a different release profile between intraliposomal drugs and liposomes. This demonstrates the need to image both drug and carrier simultaneously and independently (Figure 5c). Another study in 2021 showed CEST imaging of a self-healing hydrogel loaded with gemcitabine (Gem) at 2.2 ppm which exhibited sustainable cytotoxicity towards the human glioblastomas cell line [167]. This chitosan-dextran (CD) based hydrogel generated inherent CEST contrast at 1.1 ppm at 3 T MRI (Figure 5d). These CEST detectable chemotherapeutics and hydrogels could be promising approaches for controlled drug release and local treatment of brain tumors under MRI guidance.

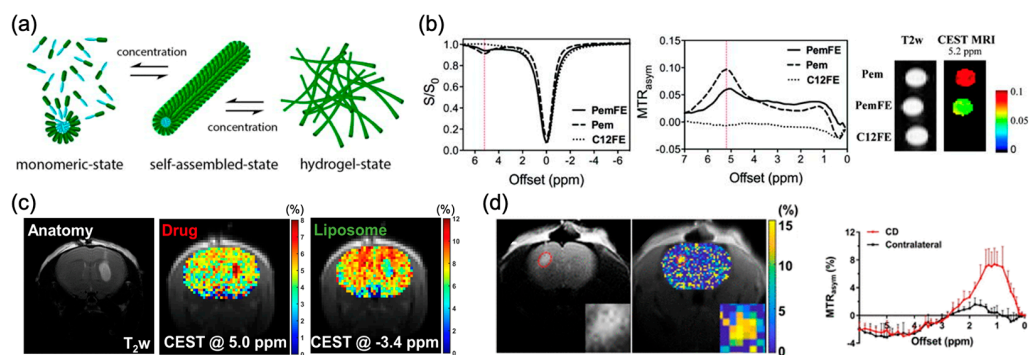


**Figure 5.** (a) Schematic illustration of the self-assembly of PemFE monomers into filamentous nanostructures that can further entangle into a 3D network for the formation of self-supporting hydrogels under suitable conditions (pH, concentration, and ionic strength). (b) Z-spectra, MTR<sub>asym</sub> plots, and CEST contrast maps of PemFE (solid), Pem (dashed), and C12FE (dotted) showing CEST peaks at 5.2 ppm. (c) T2-weighted image and CEST images (5.0 ppm and  $-3.4$  ppm) of drug barbituric acid (BA) loaded liposomal hydrogels in a mouse brain. (d) T2-weighted image, MTR<sub>asym</sub> image at 1.1 ppm, and the average MTR<sub>asym</sub> spectra of CD hydrogel in a mouse brain. Pem: Pemetrexed. Reproduced with permission from [159], American Chemical Society, 2017 [166], Ivyspring International Publisher, 2020 [167], American Chemical Society, 2021.

## 5. Technical Part

CEST contrast is dependent on acquisitions and post-processing methods. In brain tumors, careful interpretation is needed since other contributions, such as MT and T1, could be quite different from normal brain tissues [10,21,25,34,89,90,96,99,100,104,168,169]. In this section, we will explain the principle of CEST acquisition, the common methods in analyzing the Z-spectrum, and recent developments in using deep-learning to assist CEST post-processing.

### 5.1. CEST Acquisition

The CEST signal is acquired by detecting the water signal after saturation of exchangeable protons of the molecules (solute) using frequency selective radio frequency (RF) pulses. This signal reduction of the exchangeable protons will then be transferred to the bulk water protons at 110 MHz [49–51]. The exchange process can be quantified by the exchange rate of  $k_{sw}$  from solute to water (or  $k_{ws}$  from the water back to solute). After saturation, the water signal is measured by common MRI sequences. The difference between saturated and unsaturated water signals can be used to quantify the solute. In typical Z-spectrum acquisition, the frequency of saturation RF pulse is swept at a range with offsets at both sides of the water signal (defined at 0 ppm), depending on the types of exchangeable protons [170]. This Z-spectrum is slightly different from conventional MRS or NMR where the water peak is at 4.7 ppm with respect to tetramethylsilane (TMS). The saturated water signal ( $S_{sat}$ ) is usually normalized to the unsaturated water signal ( $S_0$ ). By analyzing the Z-spectrum, the CEST contrast of the molecule can be obtained.

The basic CEST sequence consists of a pre-saturation module and an image readout module [46,50,52,169]. The pre-saturation module is to label the exchanging protons using an irradiation field with an amplitude of  $B_1$ , a duration of  $t_{sat}$ , and a frequency offset of  $\Delta\omega$  with respect to water signal at 0 ppm. The  $B_1$  and  $t_{sat}$  are closely related to CEST sensitivity and typically require optimization for a specific CEST study. In the CEST field, the commonly used saturation module is either a continuous-wave CEST/spin lock or pulsed CEST [52], while a pulsed CEST is currently more preferred in clinical applications because of special absorption rate (SAR) limitations. Pulsed CEST has another advantage of suppressing the MT effect [81,97]. Theoretically, the readout module can be any MRI sequence that includes excitation, spatial encoding, and data acquisition. With considerations of both signal-to-noise ratio (SNR) and scan time, the commonly used image

readout module in CEST is turbo spin echo (TSE), also known as fast spin echo (FSE) or rapid acquisition with relaxation enhancement (RARE).

## 5.2. CEST Post-Processing

### 5.2.1. Z-Spectra and $B_0/B_1$ Correction

CEST MRI requires specific post-processing to obtain contrasts. After acquiring CEST data, Z-spectra can be obtained by following equation [50,52]:

$$Z(\Delta\omega) = \frac{S_{sat}(\Delta\omega)}{S_0}, \quad (1)$$

where  $\Delta\omega$  represents the frequency offset with respect to the water frequency at 0 ppm,  $S_{sat}(\Delta\omega)$  and  $S_0$  are the steady-state magnetization with saturation at  $\Delta\omega$  and without saturation, respectively. Since the quantification of Z-spectra is exquisitely sensitive to static magnetic field ( $B_0$ ) inhomogeneity, which exists in most MRI scanners,  $B_0$  correction is needed. Typically  $B_0$  correction is performed in two steps: (i) Generate a  $B_0$  map: the  $B_0$  map can be obtained by estimating the minimum of interpolated/fitted Z-spectra [48,171,172], water saturation shift referencing (WASSR) [173], or other  $B_0$  mapping methods [174–176]. The latter two require extra data acquisition in addition to CEST data. (ii) Correct  $B_0$  inhomogeneity for Z-spectra: the frequency shift values on  $B_0$  map are applied to correct the corresponding Z-spectra on a pixel-by-pixel basis. After  $B_0$  correction, it is sometimes suggested performing  $B_1$  correction if the scanner has large  $B_1$  inhomogeneity [35,176]. Similar to  $B_0$  correction,  $B_1$  correction includes two steps: (i) Generate  $B_1$  map: the  $B_1$  map can be acquired using flip-angle mapping [35,177], double angle method (DAM) [174,178], or other  $B_1$  mapping methods [175,176]. (ii) Correct  $B_0$  inhomogeneity for Z-spectra or CEST contrasts: the relative values on  $B_1$  map are applied to correct the corresponding Z-spectra or CEST contrasts on a pixel-by-pixel basis. Notably, whether to correct  $B_0$  or  $B_1$  depends on the scanner used for data collection and the analysis method used to extract CEST contrasts. Finally, the Z-spectra are analyzed to obtain the CEST contrast. Z-spectra analysis methods can be categorized into three types, i.e., Z-spectra analysis, Inverse Z-spectra analysis, and deep-learning methods.

### 5.2.2. Z-Spectra Analysis

Conventional Z-spectrum analysis can be summarized as quantifying the CEST contrasts using the difference between the acquired Z-spectrum ( $Z$ ) from the reference spectrum ( $Z_{ref}$ ). Currently, many methods, including  $MTR_{asym}$  [47,48], Lorentzian difference (LD) [44,179], multi-pool Lorentzian fitting [180,181], polynomial and Lorentzian line-shape fitting (PLOF) [182–184], and three-offset method [93,185,186] have been applied in different CEST studies.

#### (1) $MTR_{asym}$ analysis

$MTR_{asym}$  analysis directly uses the signal at symmetrical frequency offsets in water frequency on Z-spectra as a reference to calculate the CEST contrasts [47,48]:

$$MTR_{asym}(\Delta\omega) = Z_{ref}(\Delta\omega) - Z(\Delta\omega) = Z(-\Delta\omega) - Z(\Delta\omega). \quad (2)$$

This method is more suitable for analyzing CEST data without CEST/MT on the negative side of Z-spectra, such as solution phantom data. When it is applied in analyzing *in vivo* data, the calculated result should be interpreted carefully as it contains multiple molecular contributions from both sides of the Z-spectrum, such as asymmetric MTC.

#### (2) Lorentzian difference analysis (LDA)

LDA first fits the *DS* effect using a Lorentzian line shape to obtain the reference spectra [44,179]:

$$Z_{ref}(\Delta\omega) = 1 - L_{DS} = 1 - \frac{A_{DS}}{1 + \left[ \frac{\Delta\omega - \delta_{DS}}{\Gamma_{DS}/2} \right]^2}, \quad (3)$$

and then subtracts the acquired *Z*-spectrum from the fitted reference curve to obtain the CEST contrasts:

$$CEST(\Delta\omega) = Z_{ref}(\Delta\omega) - Z(\Delta\omega) = 1 - \frac{A_{DS}}{1 + \left[ \frac{\Delta\omega - \delta_{DS}}{\Gamma_{DS}/2} \right]^2} - Z(\Delta\omega), \quad (4)$$

where  $A_{DS}$  represents the water peak amplitude,  $\Gamma_{DS}$  is the full-width-at-half-maximum (FWHM) of water peak, and  $\delta_{DS}$  is the water peak position (can be set to 0 ppm after  $B_0$  correction). For *in vivo* study, MT contrast may affect interested CEST contrasts (especially NOE) and thus can be excluded from the  $Z_{ref}$ . In this case, an MT term ( $L_{MT}$ ) is additionally subtracted from Equation (3) [187].

### (3) Multi-pool Lorentzian fitting

Multi-pool Lorentzian fitting is another Lorentzian-based method for analyzing the *Z*-spectrum [180]. With each pool taken as a Lorentzian line shape, the fitted *Z*-spectrum can be expressed as:

$$Z_{fit}(\Delta\omega) = 1 - \sum_{i=1}^n L_i(\Delta\omega). \quad (5)$$

$L_i$  refers to all peaks that contribute to the *Z*-spectra, including all CEST, DS, and MT peaks:

$$L_i(\Delta\omega) = \frac{A_i}{1 + \left( \frac{\Delta\omega - \delta_i}{\Gamma_i/2} \right)^2} \quad (6)$$

where  $A_i$ ,  $\Gamma_i$ , and  $\delta_i$  refer to the amplitude, FWHM, and position of each peak, respectively. For multi-pool Lorentzian fitting, the  $Z_{ref}$  of pool  $i$  can be expressed as:

$$Z_{ref,i}(\Delta\omega) = 1 - \sum_{j \neq i}^n L_j(\Delta\omega), \quad \{1 \leq j \leq n\}. \quad (7)$$

It is worth noting that the initial values and boundary values may affect the accuracy of multi-pool Lorentzian fitting and thus need to be defined properly [181]. At low field strength, some CEST peaks overlap with adjacent peaks, thus the total pool numbers need to be adjusted accordingly [99,188].

### (4) Polynomial and Lorentzian line-shape fitting (PLOF)

PLOF is a CEST analysis method that combines Lorentzian fitting for CEST signal ( $R_{ex}$ ) with N-order polynomial fitting for background signal ( $R_{back}$ ) [182–184]:

$$R_{ex}(\Delta\omega) = \frac{R_{ex}^{max}}{1 + \left( \frac{\Delta\omega - \delta}{\Gamma_i/2} \right)^2}, \quad (8)$$

$$R_{back}(\Delta\omega) = \sum_{n=1}^N C_n (\Delta\omega - \delta)^n, \quad (9)$$

where  $C_n$  is the coefficient of the  $n$ -th order. After fitting, the observed CEST contrast is calculated by:

$$CEST(\Delta\omega) = Z(R_{eff} + R_{back}) - Z(R_{eff} + R_{back} + R_{ex}) \quad (10)$$

where  $R_{eff}$  is the measured longitudinal relaxation rate of water in the rotating frame without additional solutes. Here, the  $Z(R_{eff} + R_{back})$  can be taken as reference signal  $Z_{ref}$  while the  $Z(R_{eff} + R_{back} + R_{ex})$  can be taken as labeled signal  $Z_{lab}$ . Currently, PLOF is mainly used to analyze creatine CEST data; it is also applicable to amide CEST with adjustment on background signal fitting [175].

### (5) Three-offset method

Some studies reported a simple three-offset method to obtain APT and NOE CEST contrasts [93,185,186], thus reducing the scan time by skipping data acquisition of some frequency offsets. The CEST contrast is calculated by:

$$CEST(\Delta\omega) = Z_{ref}(\Delta\omega) - Z(\Delta\omega) = \frac{Z(\Delta\omega - \delta\omega) + Z(\Delta\omega + \delta\omega)}{2} - Z(\Delta\omega) \quad (11)$$

where  $\delta\omega$  refers to the frequency offset with respect to  $\Delta\omega$  and can be set to different values for different CEST contrast at different field strengths. The three-offset method is more suitable for CEST studies at high fields as it relies on a clear delineation of CEST peaks [185].

### 5.2.3. Inverse Z-Spectra Analysis

Endogenous CEST effects close to 0 ppm are easily attenuated by the DS and MT effects. Zaiss et al. proposed to analyze Z-spectrum inversely to obtain the CEST contrasts with correction of these effects [34,189]:

$$CEST_{Rex} = \frac{1}{Z_{lab}} - \frac{1}{Z_{ref, i}}, \quad (12)$$

where  $Z_{lab}$  and  $Z_{ref}$  represent the Z-spectrum values of label and reference, respectively. The  $Z_{ref}$  can be calculated using the above-mentioned five methods in Section 5.2.2, the  $Z_{lab}$  is the acquired (labeled) Z-spectra data. Moreover, CEST contrast is also affected by the longitudinal relaxation time ( $T_1$ ) of water. To address this problem, AREX contrast, which excludes  $T_1$  contributions, can be used to calculate the CEST signal that more represents chemical exchange than conventional CEST analysis [34,189]. The AREX contrast is calculated by:

$$AREX = CEST_{Rex} \cdot R_1 = \left( \frac{1}{Z_{lab}} - \frac{1}{Z_{ref, i}} \right) \cdot R_1, \quad (13)$$

where  $R_1$  ( $1/T_1$ ) refers to the longitudinal relaxation rate.

### 5.2.4. Deep Learning-Based Analysis Methods

Recently, deep learning-based methods [15,99,100,104,188,190,191] have also been applied to obtain CEST contrasts to speed up and simplify the post-processing of CEST. Deep learning utilizes neural networks that are composed of multiple processing layers to extract information from data [192].

#### (1) Deep learning-based Z-spectra analysis

In the presence of the scaling effects from the MT effect and DS, some CEST peaks cannot be clearly identified, especially at a low magnetic field (3 T or less). Zaiss et al. proposed to predict 9.4 T CEST signals from 3 T CEST signals using a deep neural network (deepCEST), demonstrating the feasibility of extracting unobservable CEST signals from low-field CEST data [100]. Glang et al. further improved the performance of deepCEST at 3 T using a probabilistic deep learning approach which provides additional information about the reliability of the prediction [99]. In addition to deepCEST, Huang et al. demonstrated that the AREX contrasts can be predicted by a deep neural network (deepAREX) which requires both Z-spectra and  $T_1$  as inputs [188]. Chen et al. utilized an artificial neural network to extract CEST properties (ANNCEST), such as metabolite concentration,

exchange rate, and  $B_0/B_1$ . The ANNCEST is sensitive to map the phosphocreatine (PCr) concentration in human skeletal muscle on a 3 T clinical scanner [15].

## (2) Deep learning-based CEST fingerprinting

Some other studies combined MR fingerprinting with a deep neural network reconstruction to obtain the molecular properties, including concentration and exchange rate [104,190,191,193]. In this case, the CEST sequence needs to be specifically designed and a simulation dictionary should be built for network training.

Despite the differences in the technical details of these methods, all the deep learning-based methods could substantially speed up the post-processing of CEST MRI (e.g., up to a second level after training). These studies all demonstrated the great potential of deep learning-based CEST analysis.

## 6. Promises and Challenges

CEST imaging of amide protons at 3.5 ppm has been successfully translated to image brain tumor patients in a short period of time due to its non-invasive nature. Other CEST contrasts indicate alterations of aliphatic protons (NOE, typically at  $-3.5$  ppm) and amine protons (at 2 ppm) could be considered collectively in diagnosis, prognosis, and assessment of the treatment effects in brain tumors. Moreover, CEST is also capable of detecting drugs approved for clinical use, such as anticancer drugs. This detection of natural labels on molecules could facilitate the development of image-guided drug delivery to the brain, especially those that can cross or bypass the BBB. Theranostic approaches could facilitate the assessment of treatment effects longitudinally and multiple component changes in drug delivery systems, such as liposomes and hydrogels.

In addition to CEST MRI, various imaging approaches provide valuable information to characterize the heterogeneity of brain tumors. For example, diffusion weighted imaging (DWI) or diffusion tensor imaging (DTI) measures the degree of water movement, thus detecting pathologies that change this movement in brain tumors [31,194,195]. Perfusion weighted imaging (PWI) using DCE, dynamic susceptibility contrast (DSC), and arterial spin labeling (ASL) is commonly used to measure cerebral hemodynamics [111,196–199]. Both diffusion and perfusion indicate structural abnormalities in tumors, such as leaky vasculature and poor drainage [200,201]. Proton  $^1H$  MRS has been used to evaluate the altered metabolism in brain tumors [202,203], though its application is limited by the limited spatial information. Other than MRI, FDG-PET is a commonly used imaging approach for tumor detection and grading as tumors typically have abnormal glucose uptake [204,205]. Compared to these clinical approaches, CEST is a sensitive and non-invasive method of detecting molecular alterations in terms of concentration and exchange environment. Majority MRI approaches characterize tumors with respect to structural alterations, FDG-PET is regarded as an invasive approach whose pros and cons can be found in Section 3. Moreover, DWI, DTI, ASL, MRS, and CEST do not require the administration of contrast agents which could support non-invasive and frequent assessments. Thus, DWI/DTI and ASL could be applied in conjunction with CEST to further characterize heterogenous brain tumors.

This uniqueness of CEST MRI has led to enthusiasm in the field, but challenges remain in clinical translations in both data acquisition and post-processing. First,  $B_1$  needs to be optimized to achieve a high labeling efficiency during acquisition for exchanging protons and the RF constraint, i.e., specific absorption rate (SAR), especially at low  $B_0$  field. Second, the CEST sequence also needs optimization because Z-spectrum acquisition requires measurements at a series of frequency offsets, which is time-consuming. Third, motion correction approaches are needed for human applications as small motion could induce error in CEST quantification. Fourth, there is no standardized method yet to analyze CEST data and there are many post-processing methods available. Finally, the interpretation of changes in CEST contrast is not straightforward. Great caution should be taken as CEST contrast depends on the molecular alterations in vivo, such as concentration and exchange rate. Moreover, brain tumors have complicated and heterogenous microenvironments, such as liquefactive

necrosis and hemorrhage. Researchers in the field are working together to standardize the CEST imaging of brain tumors. Recent developments in pulse sequences [175,206–210] that strive to achieve high SNR, whole-brain coverage, and short acquisition time, together with the deep learning-based analysis, are expected to open new avenues for realizing fast and accurate CEST MRI.

## 7. Conclusions

CEST MRI is a promising non-invasive imaging method to detect molecules at the millimolar level. Great promise has been shown in the grading of brain tumors, potential identification mutation, and regional changes, such as radiation necrosis, cellularity, and IDH. CEST MRI also enables the detection of therapeutics, liposome-based, and hydrogel-based drug delivery. These theranostic applications could provide valuable information for the adjustment of treatments, demonstrating the potential for precision medicine. Both the acquisition and post-processing of CEST are not so trivial and could be addressed by using a specific pulse sequence design and deep learning-based analysis. When more preclinical and clinical studies become available, technical hurdles may be overcome to bring this promising field to wide neuroimaging applications.

**Author Contributions:** Literature review, K.W.Y.C., J.H., Z.C., S.-W.P. and J.H.C.L.; writing—original draft preparation, K.W.Y.C., J.H., Z.C., S.-W.P. and J.H.C.L.; writing—review and editing, K.W.Y.C., J.H. and Z.C.; supervision, K.W.Y.C.; funding acquisition, K.W.Y.C. All authors have read and agreed to the published version of the manuscript.

**Funding:** This research was funded by the Research Grants Council: 11102218, PDFS2122-1S01; City University of Hong Kong: 7005433, 7005626 and 96667198; the National Natural Science Foundation of China: 81871409; Tung Biomedical Science Centre; and the Hong Kong Centre for Cerebro-cardiovascular Health Engineering. The APC was funded by City University of Hong Kong: 7005433.

**Institutional Review Board Statement:** Not applicable.

**Informed Consent Statement:** Not applicable.

**Data Availability Statement:** Not applicable.

**Conflicts of Interest:** The authors declare no conflict of interest.

## References

1. Sanvito, F.; Castellano, A.; Falini, A. Advancements in Neuroimaging to Unravel Biological and Molecular Features of Brain Tumors. *Cancers* **2021**, *13*, 424. [[CrossRef](#)] [[PubMed](#)]
2. Gritsch, S.; Batchelor, T.T.; Gonzalez Castro, L.N. Diagnostic, therapeutic, and prognostic implications of the 2021 World Health Organization classification of tumors of the central nervous system. *Cancer* **2022**, *128*, 47–58. [[CrossRef](#)] [[PubMed](#)]
3. Zhou, J.; Lal, B.; Wilson, D.A.; Laterra, J.; van Zijl, P.C. Amide proton transfer (APT) contrast for imaging of brain tumors. *Magn. Reson. Med.* **2003**, *50*, 1120–1126. [[CrossRef](#)] [[PubMed](#)]
4. Jones, C.K.; Schlosser, M.J.; van Zijl, P.C.; Pomper, M.G.; Golay, X.; Zhou, J. Amide proton transfer imaging of human brain tumors at 3 T. *Magn. Reson. Med.* **2006**, *56*, 585–592. [[CrossRef](#)] [[PubMed](#)]
5. Su, C.; Xu, S.; Lin, D.; He, H.; Chen, Z.; Damen, F.C.; Ke, C.; Lv, X.; Cai, K. Multi-parametric Z-spectral MRI may have a good performance for glioma stratification in clinical patients. *Eur. Radiol.* **2022**, *32*, 101–111. [[CrossRef](#)] [[PubMed](#)]
6. Zhuo, Z.; Qu, L.; Zhang, P.; Duan, Y.; Cheng, D.; Xu, X.; Sun, T.; Ding, J.; Xie, C.; Liu, X.; et al. Prediction of H3K27M-mutant brainstem glioma by amide proton transfer-weighted imaging and its derived radiomics. *Eur. J. Nucl. Med. Mol. Imaging* **2021**, *48*, 4426–4436. [[CrossRef](#)]
7. Zhang, H.; Zhou, J.; Peng, Y. Amide Proton Transfer-Weighted MR Imaging of Pediatric Central Nervous System Diseases. *Magn. Reson. Imaging Clin. N. Am.* **2021**, *29*, 631–641. [[CrossRef](#)]
8. Zhang, H.; Yong, X.; Ma, X.; Zhao, J.; Shen, Z.; Chen, X.; Tian, F.; Chen, W.; Wu, D.; Zhang, Y. Differentiation of low- and high-grade pediatric gliomas with amide proton transfer imaging: Added value beyond quantitative relaxation times. *Eur. Radiol.* **2021**, *31*, 9110–9119. [[CrossRef](#)]
9. Xu, Z.; Ke, C.; Liu, J.; Xu, S.; Han, L.; Yang, Y.; Qian, L.; Liu, X.; Zheng, H.; Lv, X.; et al. Diagnostic performance between MR amide proton transfer (APT) and diffusion kurtosis imaging (DKI) in glioma grading and IDH mutation status prediction at 3T. *Eur. J. Radiol.* **2021**, *134*, 109466. [[CrossRef](#)]
10. Wu, Y.; Liu, Z.; Yang, Q.; Zou, L.; Zhang, F.; Qian, L.; Liu, X.; Zheng, H.; Luo, D.; Sun, P.Z. Fast and equilibrium CEST imaging of brain tumor patients at 3T. *Neuroimage Clin.* **2021**, *33*, 102890. [[CrossRef](#)]

11. Warnert, E.A.H.; Wood, T.C.; Incekara, F.; Barker, G.J.; Vincent, A.J.P.; Schouten, J.; Kros, J.M.; van den Bent, M.; Smits, M.; Tamames, J.A.H. Mapping tumour heterogeneity with pulsed 3D CEST MRI in non-enhancing glioma at 3T. *MAGMA* **2021**. [[CrossRef](#)] [[PubMed](#)]
12. Sartoretti, E.; Sartoretti, T.; Wyss, M.; Reischauer, C.; van Smoorenburg, L.; Binkert, C.A.; Sartoretti-Schefer, S.; Mannil, M. Amide proton transfer weighted (APTw) imaging based radiomics allows for the differentiation of gliomas from metastases. *Sci. Rep.* **2021**, *11*, 5506. [[CrossRef](#)] [[PubMed](#)]
13. Park, J.E.; Kim, H.S.; Park, S.Y.; Jung, S.C.; Kim, J.H.; Heo, H.Y. Identification of Early Response to Anti-Angiogenic Therapy in Recurrent Glioblastoma: Amide Proton Transfer-weighted and Perfusion-weighted MRI compared with Diffusion-weighted MRI. *Radiology* **2020**, *295*, 397–406. [[CrossRef](#)] [[PubMed](#)]
14. Liu, J.; Li, C.; Chen, Y.; Lv, X.; Lv, Y.; Zhou, J.; Xi, S.; Dou, W.; Qian, L.; Zheng, H.; et al. Diagnostic performance of multiparametric MRI in the evaluation of treatment response in glioma patients at 3T. *J. Magn. Reson. Imaging* **2020**, *51*, 1154–1161. [[CrossRef](#)]
15. Chen, L.; Schär, M.; Chan, K.W.; Huang, J.; Wei, Z.; Lu, H.; Qin, Q.; Weiss, R.G.; van Zijl, P.C.; Xu, J. In vivo imaging of phosphocreatine with artificial neural networks. *Nat. Commun.* **2020**, *11*, 1–10. [[CrossRef](#)]
16. Paech, D.; Dreher, C.; Regnery, S.; Meissner, J.E.; Goerke, S.; Windschuh, J.; Oberholzner, J.; Schultheiss, M.; Deike-Hofmann, K.; Bickelhaupt, S.; et al. Relaxation-compensated amide proton transfer (APT) MRI signal intensity is associated with survival and progression in high-grade glioma patients. *Eur. Radiol.* **2019**, *29*, 4957–4967. [[CrossRef](#)]
17. Joo, B.; Han, K.; Ahn, S.S.; Choi, Y.S.; Chang, J.H.; Kang, S.G.; Kim, S.H.; Zhou, J.; Lee, S.K. Amide proton transfer imaging might predict survival and IDH mutation status in high-grade glioma. *Eur. Radiol.* **2019**, *29*, 6643–6652. [[CrossRef](#)]
18. Jiang, S.; Eberhart, C.G.; Lim, M.; Heo, H.Y.; Zhang, Y.; Blair, L.; Wen, Z.; Holdhoff, M.; Lin, D.; Huang, P.; et al. Identifying Recurrent Malignant Glioma after Treatment Using Amide Proton Transfer-Weighted MR Imaging: A Validation Study with Image-Guided Stereotactic Biopsy. *Clin. Cancer Res.* **2019**, *25*, 552–561. [[CrossRef](#)]
19. Zhang, J.; Zhu, W.; Tain, R.; Zhou, X.J.; Cai, K. Improved Differentiation of Low-Grade and High-Grade Gliomas and Detection of Tumor Proliferation Using APT Contrast Fitted from Z-Spectrum. *Mol. Imaging Biol.* **2018**, *20*, 623–631. [[CrossRef](#)]
20. Su, L.; Gao, P.; Lin, S.; Wu, B.; Qin, W.; Lin, Y.; Xue, J. Predicting O6-Methylguanine-DNA Methyltransferase Protein Expression in Primary Low- and High-Grade Gliomas Using Certain Qualitative Characteristics of Amide Proton Transfer-Weighted Magnetic Resonance Imaging. *World Neurosurg.* **2018**, *116*, e814–e823. [[CrossRef](#)]
21. Regnery, S.; Adeberg, S.; Dreher, C.; Oberholzner, J.; Meissner, J.E.; Goerke, S.; Windschuh, J.; Deike-Hofmann, K.; Bickelhaupt, S.; Zaiss, M.; et al. Chemical exchange saturation transfer MRI serves as predictor of early progression in glioblastoma patients. *Oncotarget* **2018**, *9*, 28772–28783. [[CrossRef](#)] [[PubMed](#)]
22. Paech, D.; Windschuh, J.; Oberholzner, J.; Dreher, C.; Sahm, F.; Meissner, J.E.; Goerke, S.; Schuenke, P.; Zaiss, M.; Regnery, S.; et al. Assessing the predictability of IDH mutation and MGMT methylation status in glioma patients using relaxation-compensated multipool CEST MRI at 7.0 T. *Neurology Oncol.* **2018**, *20*, 1661–1671. [[CrossRef](#)] [[PubMed](#)]
23. Joo, B.; Han, K.; Choi, Y.S.; Lee, S.K.; Ahn, S.S.; Chang, J.H.; Kang, S.G.; Kim, S.H.; Zhou, J. Amide proton transfer imaging for differentiation of benign and atypical meningiomas. *Eur. Radiol.* **2018**, *28*, 331–339. [[CrossRef](#)] [[PubMed](#)]
24. Jiang, S.; Rui, Q.; Wang, Y.; Heo, H.Y.; Zou, T.; Yu, H.; Zhang, Y.; Wang, X.; Du, Y.; Wen, X.; et al. Discriminating MGMT promoter methylation status in patients with glioblastoma employing amide proton transfer-weighted MRI metrics. *Eur. Radiol.* **2018**, *28*, 2115–2123. [[CrossRef](#)]
25. Zaiss, M.; Windschuh, J.; Goerke, S.; Paech, D.; Meissner, J.E.; Burth, S.; Kickingereder, P.; Wick, W.; Bendszus, M.; Schlemmer, H.P.; et al. Downfield-NOE-suppressed amide-CEST-MRI at 7 Tesla provides a unique contrast in human glioblastoma. *Magn. Reson. Med.* **2017**, *77*, 196–208. [[CrossRef](#)]
26. Zhou, I.Y.; Wang, E.; Cheung, J.S.; Lu, D.; Ji, Y.; Zhang, X.; Fulci, G.; Sun, P.Z. Direct saturation-corrected chemical exchange saturation transfer MRI of glioma: Simplified decoupling of amide proton transfer and nuclear overhauser effect contrasts. *Magn. Reson. Med.* **2017**, *78*, 2307–2314. [[CrossRef](#)]
27. Su, C.; Liu, C.; Zhao, L.; Jiang, J.; Zhang, J.; Li, S.; Zhu, W.; Wang, J. Amide Proton Transfer Imaging Allows Detection of Glioma Grades and Tumor Proliferation: Comparison with Ki-67 Expression and Proton MR Spectroscopy Imaging. *AJNR Am. J. Neuroradiol.* **2017**, *38*, 1702–1709. [[CrossRef](#)]
28. Ma, X.; Bai, Y.; Lin, Y.; Hong, X.; Liu, T.; Ma, L.; Haacke, E.M.; Zhou, J.; Wang, J.; Wang, M. Amide proton transfer magnetic resonance imaging in detecting intracranial hemorrhage at different stages: A comparative study with susceptibility weighted imaging. *Sci. Rep.* **2017**, *7*, 45696. [[CrossRef](#)]
29. Jiang, S.; Zou, T.; Eberhart, C.G.; Villalobos, M.A.V.; Heo, H.Y.; Zhang, Y.; Wang, Y.; Wang, X.; Yu, H.; Du, Y.; et al. Predicting IDH mutation status in grade II gliomas using amide proton transfer-weighted (APTw) MRI. *Magn. Reson. Med.* **2017**, *78*, 1100–1109. [[CrossRef](#)]
30. Jiang, S.; Eberhart, C.G.; Zhang, Y.; Heo, H.Y.; Wen, Z.; Blair, L.; Qin, H.; Lim, M.; Quinones-Hinojosa, A.; Weingart, J.D.; et al. Amide proton transfer-weighted magnetic resonance image-guided stereotactic biopsy in patients with newly diagnosed gliomas. *Eur. J. Cancer* **2017**, *83*, 9–18. [[CrossRef](#)]
31. Choi, Y.S.; Ahn, S.S.; Lee, S.K.; Chang, J.H.; Kang, S.G.; Kim, S.H.; Zhou, J. Amide proton transfer imaging to discriminate between low- and high-grade gliomas: Added value to apparent diffusion coefficient and relative cerebral blood volume. *Eur. Radiol.* **2017**, *27*, 3181–3189. [[CrossRef](#)] [[PubMed](#)]

32. Park, J.E.; Kim, H.S.; Park, K.J.; Kim, S.J.; Kim, J.H.; Smith, S.A. Pre- and Posttreatment Glioma: Comparison of Amide Proton Transfer Imaging with MR Spectroscopy for Biomarkers of Tumor Proliferation. *Radiology* **2016**, *278*, 514–523. [CrossRef] [PubMed]
33. Heo, H.Y.; Jones, C.K.; Hua, J.; Yadav, N.; Agarwal, S.; Zhou, J.; van Zijl, P.C.; Pillai, J.J. Whole-brain amide proton transfer (APT) and nuclear overhauser enhancement (NOE) imaging in glioma patients using low-power steady-state pulsed chemical exchange saturation transfer (CEST) imaging at 7T. *J. Magn. Reson. Imaging* **2016**, *44*, 41–50. [CrossRef]
34. Zaiss, M.; Windschuh, J.; Paech, D.; Meissner, J.E.; Burth, S.; Schmitt, B.; Kickingereder, P.; Wiestler, B.; Wick, W.; Bendszus, M.; et al. Relaxation-compensated CEST-MRI of the human brain at 7T: Unbiased insight into NOE and amide signal changes in human glioblastoma. *Neuroimage* **2015**, *112*, 180–188. [CrossRef]
35. Windschuh, J.; Zaiss, M.; Meissner, J.E.; Paech, D.; Radbruch, A.; Ladd, M.E.; Bachert, P. Correction of B1-inhomogeneities for relaxation-compensated CEST imaging at 7 T. *NMR Biomed.* **2015**, *28*, 529–537. [CrossRef] [PubMed]
36. Togao, O.; Hiwatashi, A.; Keupp, J.; Yamashita, K.; Kikuchi, K.; Yoshiura, T.; Suzuki, Y.; Kruiskamp, M.J.; Sagiyama, K.; Takahashi, M.; et al. Scan-rescan reproducibility of parallel transmission based amide proton transfer imaging of brain tumors. *J. Magn. Reson. Imaging* **2015**, *42*, 1346–1353. [CrossRef] [PubMed]
37. Paech, D.; Burth, S.; Windschuh, J.; Meissner, J.E.; Zaiss, M.; Eidel, O.; Kickingereder, P.; Nowosielski, M.; Wiestler, B.; Sahm, F.; et al. Nuclear Overhauser Enhancement imaging of glioblastoma at 7 Tesla: Region specific correlation with apparent diffusion coefficient and histology. *PLoS ONE* **2015**, *10*, e0121220. [CrossRef]
38. Harris, R.J.; Cloughesy, T.F.; Liau, L.M.; Prins, R.M.; Antonios, J.P.; Li, D.; Yong, W.H.; Pope, W.B.; Lai, A.; Nghiemphu, P.L.; et al. pH-weighted molecular imaging of gliomas using amine chemical exchange saturation transfer MRI. *Neurol Oncol.* **2015**, *17*, 1514–1524. [CrossRef]
39. Togao, O.; Yoshiura, T.; Keupp, J.; Hiwatashi, A.; Yamashita, K.; Kikuchi, K.; Suzuki, Y.; Suzuki, S.O.; Iwaki, T.; Hata, N.; et al. Amide proton transfer imaging of adult diffuse gliomas: Correlation with histopathological grades. *Neurol Oncol.* **2014**, *16*, 441–448. [CrossRef]
40. Sagiyama, K.; Mashimo, T.; Togao, O.; Vemireddy, V.; Hatanpaa, K.J.; Maher, E.A.; Mickey, B.E.; Pan, E.; Sherry, A.D.; Bachoo, R.M.; et al. In vivo chemical exchange saturation transfer imaging allows early detection of a therapeutic response in glioblastoma. *Proc. Natl. Acad. Sci. USA* **2014**, *111*, 4542–4547. [CrossRef]
41. Paech, D.; Zaiss, M.; Meissner, J.E.; Windschuh, J.; Wiestler, B.; Bachert, P.; Neumann, J.O.; Kickingereder, P.; Schlemmer, H.P.; Wick, W.; et al. Nuclear overhauser enhancement mediated chemical exchange saturation transfer imaging at 7 Tesla in glioblastoma patients. *PLoS ONE* **2014**, *9*, e104181. [CrossRef] [PubMed]
42. Zhou, J.; Zhu, H.; Lim, M.; Blair, L.; Quinones-Hinojosa, A.; Messina, S.A.; Eberhart, C.G.; Pomper, M.G.; Laterra, J.; Barker, P.B.; et al. Three-dimensional amide proton transfer MR imaging of gliomas: Initial experience and comparison with gadolinium enhancement. *J. Magn. Reson. Imaging* **2013**, *38*, 1119–1128. [CrossRef] [PubMed]
43. Zhou, J.; Hong, X.; Zhao, X.; Gao, J.H.; Yuan, J. APT-weighted and NOE-weighted image contrasts in glioma with different RF saturation powers based on magnetization transfer ratio asymmetry analyses. *Magn. Reson. Med.* **2013**, *70*, 320–327. [CrossRef] [PubMed]
44. Jones, C.K.; Huang, A.; Xu, J.; Edden, R.A.; Schar, M.; Hua, J.; Oskolkov, N.; Zaca, D.; Zhou, J.; McMahon, M.T.; et al. Nuclear Overhauser enhancement (NOE) imaging in the human brain at 7T. *NeuroImage* **2013**, *77*, 114–124. [CrossRef] [PubMed]
45. Wen, Z.; Hu, S.; Huang, F.; Wang, X.; Guo, L.; Quan, X.; Wang, S.; Zhou, J. MR imaging of high-grade brain tumors using endogenous protein and peptide-based contrast. *Neuroimage* **2010**, *51*, 616–622. [CrossRef]
46. Ward, K.; Aletras, A.; Balaban, R.S. A new class of contrast agents for MRI based on proton chemical exchange dependent saturation transfer (CEST). *J. Magn. Reson.* **2000**, *143*, 79–87. [CrossRef]
47. Zhou, J.; Van Zijl, P.C. Chemical exchange saturation transfer imaging and spectroscopy. *Prog. Nucl. Magn. Reson. Spectrosc.* **2006**, *48*, 109–136. [CrossRef]
48. Zhou, J.; Payen, J.-F.; Wilson, D.A.; Traystman, R.J.; van Zijl, P.C. Using the amide proton signals of intracellular proteins and peptides to detect pH effects in MRI. *Nat. Med.* **2003**, *9*, 1085–1090. [CrossRef]
49. Sherry, A.D.; Woods, M. Chemical exchange saturation transfer contrast agents for magnetic resonance imaging. *Annu. Rev. Biomed. Eng.* **2008**, *10*, 391–411. [CrossRef]
50. Van Zijl, P.C.; Yadav, N.N. Chemical exchange saturation transfer (CEST): What is in a name and what isn't? *Magn. Reson. Med.* **2011**, *65*, 927–948. [CrossRef]
51. Liu, G.; Song, X.; Chan, K.W.; McMahon, M.T. Nuts and bolts of chemical exchange saturation transfer MRI. *NMR Biomed.* **2013**, *26*, 810–828. [CrossRef] [PubMed]
52. Zaiss, M.; Bachert, P. Chemical exchange saturation transfer (CEST) and MR Z-spectroscopy in vivo: A review of theoretical approaches and methods. *Phys. Med. Biol.* **2013**, *58*, R221. [CrossRef] [PubMed]
53. Zhou, J.; Payen, J.F.; van Zijl, P.C. The interaction between magnetization transfer and blood-oxygen-level-dependent effects. *Magn. Reson. Med.* **2005**, *53*, 356–366. [CrossRef]
54. van Zijl, P.C.M.; Brindle, K.; Lu, H.; Barker, P.B.; Edden, R.; Yadav, N.; Knutsson, L. Hyperpolarized MRI, functional MRI, MR spectroscopy and CEST to provide metabolic information in vivo. *Curr. Opin. Chem. Biol.* **2021**, *63*, 209–218. [CrossRef] [PubMed]
55. Mitchell, M.J.; Jain, R.K.; Langer, R. Engineering and physical sciences in oncology: Challenges and opportunities. *Nat. Rev. Cancer* **2017**, *17*, 659–675. [CrossRef] [PubMed]

56. Dewhirst, M.W.; Secomb, T.W. Transport of drugs from blood vessels to tumour tissue. *Nat. Rev. Cancer* **2017**, *17*, 738–750. [[CrossRef](#)]
57. De Palma, M.; Biziato, D.; Petrova, T.V. Microenvironmental regulation of tumour angiogenesis. *Nat. Rev. Cancer* **2017**, *17*, 457–474. [[CrossRef](#)]
58. Corbet, C.; Feron, O. Tumour acidosis: From the passenger to the driver's seat. *Nat. Rev. Cancer* **2017**, *17*, 577–593. [[CrossRef](#)]
59. Schon, S.; Cabello, J.; Liesche-Starnecker, F.; Molina-Romero, M.; Eichinger, P.; Metz, M.; Karimov, I.; Preibisch, C.; Keupp, J.; Hock, A.; et al. Imaging glioma biology: Spatial comparison of amino acid PET, amide proton transfer, and perfusion-weighted MRI in newly diagnosed gliomas. *Eur. J. Nucl. Med. Mol. Imaging* **2020**, *47*, 1468–1475. [[CrossRef](#)]
60. Zhou, J.; Blakeley, J.O.; Hua, J.; Kim, M.; Laterra, J.; Pomper, M.G.; van Zijl, P.C. Practical data acquisition method for human brain tumor amide proton transfer (APT) imaging. *Magn. Reson. Med.* **2008**, *60*, 842–849. [[CrossRef](#)]
61. Durmo, F.; Rydhog, A.; Testud, F.; Latt, J.; Schmitt, B.; Rydelius, A.; Englund, E.; Bengzon, J.; van Zijl, P.; Knutsson, L.; et al. Assessment of Amide proton transfer weighted (APTw) MRI for pre-surgical prediction of final diagnosis in gliomas. *PLoS ONE* **2020**, *15*, e0244003. [[CrossRef](#)] [[PubMed](#)]
62. Zou, T.; Yu, H.; Jiang, C.; Wang, X.; Jiang, S.; Rui, Q.; Mei, Y.; Zhou, J.; Wen, Z. Differentiating the histologic grades of gliomas preoperatively using amide proton transfer-weighted (APTw) and intravoxel incoherent motion MRI. *NMR Biomed.* **2018**, *31*, e3850. [[CrossRef](#)] [[PubMed](#)]
63. Bai, Y.; Lin, Y.; Zhang, W.; Kong, L.; Wang, L.; Zuo, P.; Vallines, I.; Schmitt, B.; Tian, J.; Song, X.; et al. Noninvasive amide proton transfer magnetic resonance imaging in evaluating the grading and cellularity of gliomas. *Oncotarget* **2017**, *8*, 5834–5842. [[CrossRef](#)] [[PubMed](#)]
64. Jiang, S.; Yu, H.; Wang, X.; Lu, S.; Li, Y.; Feng, L.; Zhang, Y.; Heo, H.Y.; Lee, D.H.; Zhou, J.; et al. Molecular MRI differentiation between primary central nervous system lymphomas and high-grade gliomas using endogenous protein-based amide proton transfer MR imaging at 3 Tesla. *Eur. Radiol.* **2016**, *26*, 64–71. [[CrossRef](#)] [[PubMed](#)]
65. Sakata, A.; Okada, T.; Yamamoto, A.; Kanagaki, M.; Fushimi, Y.; Okada, T.; Dodo, T.; Arakawa, Y.; Schmitt, B.; Miyamoto, S.; et al. Grading glial tumors with amide proton transfer MR imaging: Different analytical approaches. *J. Neurooncol.* **2015**, *122*, 339–348. [[CrossRef](#)]
66. Albatany, M.; Ostapchenko, V.G.; Meakin, S.; Bartha, R. Brain tumor acidification using drugs simultaneously targeting multiple pH regulatory mechanisms. *J. Neurooncol.* **2019**, *144*, 453–462. [[CrossRef](#)]
67. Meissner, J.E.; Korzowski, A.; Regnery, S.; Goerke, S.; Breitling, J.; Floca, R.O.; Debus, J.; Schlemmer, H.P.; Ladd, M.E.; Bachert, P.; et al. Early response assessment of glioma patients to definitive chemoradiotherapy using chemical exchange saturation transfer imaging at 7 T. *J. Magn. Reson. Imaging* **2019**, *50*, 1268–1277. [[CrossRef](#)]
68. Ma, B.; Blakeley, J.O.; Hong, X.; Zhang, H.; Jiang, S.; Blair, L.; Zhang, Y.; Heo, H.Y.; Zhang, M.; van Zijl, P.C.; et al. Applying amide proton transfer-weighted MRI to distinguish pseudoprogression from true progression in malignant gliomas. *J. Magn. Reson. Imaging* **2016**, *44*, 456–462. [[CrossRef](#)]
69. Hong, X.; Liu, L.; Wang, M.; Ding, K.; Fan, Y.; Ma, B.; Lal, B.; Tyler, B.; Mangraviti, A.; Wang, S.; et al. Quantitative multiparametric MRI assessment of glioma response to radiotherapy in a rat model. *Neuro Oncol.* **2014**, *16*, 856–867. [[CrossRef](#)]
70. Zhou, J.; Tryggestad, E.; Wen, Z.; Lal, B.; Zhou, T.; Grossman, R.; Wang, S.; Yan, K.; Fu, D.X.; Ford, E.; et al. Differentiation between glioma and radiation necrosis using molecular magnetic resonance imaging of endogenous proteins and peptides. *Nat. Med.* **2011**, *17*, 130–134. [[CrossRef](#)]
71. Han, Y.; Wang, W.; Yang, Y.; Sun, Y.Z.; Xiao, G.; Tian, Q.; Zhang, J.; Cui, G.B.; Yan, L.F. Amide Proton Transfer Imaging in Predicting Isocitrate Dehydrogenase 1 Mutation Status of Grade II/III Gliomas Based on Support Vector Machine. *Front. Neurosci.* **2020**, *14*, 144. [[CrossRef](#)] [[PubMed](#)]
72. Wang, Y.L.; Yao, J.; Chakhoyan, A.; Raymond, C.; Salamon, N.; Liau, L.M.; Nghiempuu, P.L.; Lai, A.; Pope, W.B.; Nguyen, N.; et al. Association between Tumor Acidity and Hypervascularity in Human Gliomas Using pH-Weighted Amine Chemical Exchange Saturation Transfer Echo-Planar Imaging and Dynamic Susceptibility Contrast Perfusion MRI at 3T. *AJNR Am. J. Neuroradiol.* **2019**, *40*, 979–986. [[CrossRef](#)] [[PubMed](#)]
73. Lindeman, L.R.; Randtke, E.A.; High, R.A.; Jones, K.M.; Howison, C.M.; Pagel, M.D. A comparison of exogenous and endogenous CEST MRI methods for evaluating in vivo pH. *Magn. Reson. Med.* **2018**, *79*, 2766–2772. [[CrossRef](#)] [[PubMed](#)]
74. Sotirios, B.; Demetriou, E.; Topriceanu, C.C.; Zakrzewska, Z. The role of APT imaging in gliomas grading: A systematic review and meta-analysis. *Eur. J. Radiol.* **2020**, *133*, 109353. [[CrossRef](#)] [[PubMed](#)]
75. Zhou, J.; Heo, H.Y.; Knutsson, L.; van Zijl, P.C.M.; Jiang, S. APT-weighted MRI: Techniques, current neuro applications, and challenging issues. *J. Magn. Reson. Imaging* **2019**, *50*, 347–364. [[CrossRef](#)] [[PubMed](#)]
76. Kamimura, K.; Nakajo, M.; Yoneyama, T.; Takumi, K.; Kumagae, Y.; Fukukura, Y.; Yoshiura, T. Amide proton transfer imaging of tumors: Theory, clinical applications, pitfalls, and future directions. *Jpn. J. Radiol.* **2019**, *37*, 109–116. [[CrossRef](#)]
77. Jones, K.M.; Pollard, A.C.; Pagel, M.D. Clinical applications of chemical exchange saturation transfer (CEST) MRI. *J. Magn. Reson. Imaging* **2018**, *47*, 11–27. [[CrossRef](#)]
78. Vinogradov, E.; Sherry, A.D.; Lenkinski, R.E. CEST: From basic principles to applications, challenges and opportunities. *J. Magn. Reson.* **2013**, *229*, 155–172. [[CrossRef](#)]
79. Kogan, F.; Hariharan, H.; Reddy, R. Chemical Exchange Saturation Transfer (CEST) Imaging: Description of Technique and Potential Clinical Applications. *Curr Radiol Rep* **2013**, *1*, 102–114. [[CrossRef](#)]

80. Ferris, S.P.; Hofmann, J.W.; Solomon, D.A.; Perry, A. Characterization of gliomas: From morphology to molecules. *Virchows. Arch.* **2017**, *471*, 257–269. [[CrossRef](#)]
81. Huang, J.; Han, X.; Chen, L.; Xu, X.; Xu, J.; Chan, K.W. Relayed nuclear Overhauser enhancement imaging with magnetization transfer contrast suppression at 3 T. *Magn. Reson. Med.* **2021**, *85*, 254–267. [[CrossRef](#)] [[PubMed](#)]
82. Goerke, S.; Soehngen, Y.; Deshmane, A.; Zaiss, M.; Breitling, J.; Boyd, P.S.; Herz, K.; Zimmermann, F.; Klika, K.D.; Schlemmer, H.P. Relaxation-compensated APT and rNOE CEST-MRI of human brain tumors at 3 T. *Magn. Reson. Med.* **2019**, *82*, 622–632. [[CrossRef](#)] [[PubMed](#)]
83. Longo, D.L.; Di Gregorio, E.; Abategiovanni, R.; Ceccon, A.; Assfalg, M.; Molinari, H.; Aime, S. Chemical exchange saturation transfer (CEST): An efficient tool for detecting molecular information on proteins' behaviour. *Analyst* **2014**, *139*, 2687–2690. [[CrossRef](#)]
84. Chen, L.; Wei, Z.; Chan, K.W.; Cai, S.; Liu, G.; Lu, H.; Wong, P.C.; van Zijl, P.C.; Li, T.; Xu, J. Protein aggregation linked to Alzheimer's disease revealed by saturation transfer MRI. *Neuroimage* **2019**, *188*, 380–390. [[CrossRef](#)] [[PubMed](#)]
85. Yadav, N.N.; Yang, X.; Li, Y.; Li, W.; Liu, G.; Van Zijl, P.C. Detection of dynamic substrate binding using MRI. *Sci. Rep.* **2017**, *7*, 1–7. [[CrossRef](#)]
86. Wang, S.; Tryggestad, E.; Zhou, T.; Armour, M.; Wen, Z.; Fu, D.X.; Ford, E.; van Zijl, P.C.; Zhou, J. Assessment of MRI parameters as imaging biomarkers for radiation necrosis in the rat brain. *Int. J. Radiat. Oncol. Biol. Phys.* **2012**, *83*, e431–e436. [[CrossRef](#)]
87. Heo, H.Y.; Zhang, Y.; Lee, D.H.; Hong, X.; Zhou, J. Quantitative assessment of amide proton transfer (APT) and nuclear overhauser enhancement (NOE) imaging with extrapolated semi-solid magnetization transfer reference (EMR) signals: Application to a rat glioma model at 4.7 Tesla. *Magn. Reson. Med.* **2016**, *75*, 137–149. [[CrossRef](#)]
88. Zhang, Y.; Heo, H.Y.; Jiang, S.; Lee, D.H.; Bottomley, P.A.; Zhou, J. Highly accelerated chemical exchange saturation transfer (CEST) measurements with linear algebraic modeling. *Magn. Reson. Med.* **2016**, *76*, 136–144. [[CrossRef](#)]
89. Heo, H.Y.; Lee, D.H.; Zhang, Y.; Zhao, X.; Jiang, S.; Chen, M.; Zhou, J. Insight into the quantitative metrics of chemical exchange saturation transfer (CEST) imaging. *Magn. Reson. Med.* **2017**, *77*, 1853–1865. [[CrossRef](#)]
90. Lee, D.H.; Heo, H.Y.; Zhang, K.; Zhang, Y.; Jiang, S.; Zhao, X.; Zhou, J. Quantitative assessment of the effects of water proton concentration and water T1 changes on amide proton transfer (APT) and nuclear overhauser enhancement (NOE) MRI: The origin of the APT imaging signal in brain tumor. *Magn. Reson. Med.* **2017**, *77*, 855–863. [[CrossRef](#)]
91. Heo, H.Y.; Zhang, Y.; Jiang, S.; Zhou, J. Influences of experimental parameters on chemical exchange saturation transfer (CEST) metrics of brain tumors using animal models at 4.7T. *Magn. Reson. Med.* **2019**, *81*, 316–330. [[CrossRef](#)] [[PubMed](#)]
92. Wu, Y.; Chen, Y.; Zhao, Y.; Yang, S.; Zhao, J.; Zhou, J.; Chen, Z.; Sun, P.Z.; Zheng, H. Direct radiofrequency saturation corrected amide proton transfer tumor MRI at 3 T. *Magn. Reson. Med.* **2019**, *81*, 2710–2719. [[CrossRef](#)] [[PubMed](#)]
93. Xu, J.; Zaiss, M.; Zu, Z.; Li, H.; Xie, J.; Gochberg, D.F.; Bachert, P.; Gore, J.C. On the origins of chemical exchange saturation transfer (CEST) contrast in tumors at 9.4 T. *NMR Biomed.* **2014**, *27*, 406–416. [[CrossRef](#)] [[PubMed](#)]
94. Zhang, X.-Y.; Wang, F.; Afzal, A.; Xu, J.; Gore, J.C.; Gochberg, D.F.; Zu, Z. A new NOE-mediated MT signal at around –1.6 ppm for detecting ischemic stroke in rat brain. *Magn. Reson. Imaging* **2016**, *34*, 1100–1106. [[CrossRef](#)]
95. Xu, J.; Yadav, N.N.; Bar-Shir, A.; Jones, C.K.; Chan, K.W.; Zhang, J.; Walczak, P.; McMahon, M.T.; van Zijl, P.C. Variable delay multi-pulse train for fast chemical exchange saturation transfer and relayed-nuclear overhauser enhancement MRI. *Magn. Reson. Med. Off. J. Soc. Magn. Reson. Med./Soc. Magn. Reson. Med.* **2013**, *71*, 1798–1812. [[CrossRef](#)] [[PubMed](#)]
96. Xu, X.; Yadav, N.N.; Zeng, H.; Jones, C.K.; Zhou, J.; van Zijl, P.C.; Xu, J. Magnetization transfer contrast-suppressed imaging of amide proton transfer and relayed nuclear overhauser enhancement chemical exchange saturation transfer effects in the human brain at 7T. *Magn. Reson. Med.* **2016**, *75*, 88–96. [[CrossRef](#)]
97. Huang, J.; Xu, J.; Lai, J.H.; Chen, Z.; Lee, C.Y.; Mak, H.K.; Chan, K.H.; Chan, K.W. Relayed nuclear Overhauser effect weighted (rNOEW) imaging identifies multiple sclerosis. *Neuro Image Clin.* **2021**, *32*, 102867. [[CrossRef](#)]
98. Zaiss, M.; Schuppert, M.; Deshmane, A.; Herz, K.; Ehses, P.; Fullbier, L.; Lindig, T.; Bender, B.; Ernemann, U.; Scheffler, K. Chemical exchange saturation transfer MRI contrast in the human brain at 9.4T. *Neuro Image* **2018**, *179*, 144–155. [[CrossRef](#)]
99. Glang, F.; Deshmane, A.; Prokudin, S.; Martin, F.; Herz, K.; Lindig, T.; Bender, B.; Scheffler, K.; Zaiss, M. DeepCEST 3T: Robust MRI parameter determination and uncertainty quantification with neural networks—Application to CEST imaging of the human brain at 3T. *Magn. Reson. Med.* **2020**, *84*, 450–466. [[CrossRef](#)]
100. Zaiss, M.; Deshmane, A.; Schuppert, M.; Herz, K.; Glang, F.; Ehses, P.; Lindig, T.; Bender, B.; Ernemann, U.; Scheffler, K. DeepCEST: 9.4 T Chemical exchange saturation transfer MRI contrast predicted from 3 T data—A proof of concept study. *Magn. Reson. Med.* **2019**, *81*, 3901–3914. [[CrossRef](#)]
101. Zu, Z.; Lin, E.C.; Louie, E.A.; Xu, J.; Li, H.; Xie, J.; Lankford, C.L.; Chekmenev, E.Y.; Swanson, S.D.; Does, M.D.; et al. Relayed nuclear Overhauser enhancement sensitivity to membrane Cho phospholipids. *Magn. Reson. Med.* **2020**, *84*, 1961–1976. [[CrossRef](#)] [[PubMed](#)]
102. Hobbs, S.K.; Shi, G.; Homer, R.; Harsh, G.; Atlas, S.W.; Bednarski, M.D. Magnetic resonance image-guided proteomics of human glioblastoma multiforme. *J. Magn. Reson. Imaging* **2003**, *18*, 530–536. [[CrossRef](#)] [[PubMed](#)]
103. Robbins, S.L.; Cotran, R.S. *Pathologic Basis of Disease*; Saunders: Christchurch, New Zealand, 1979.
104. Perlman, O.; Ito, H.; Herz, K.; Shono, N.; Nakashima, H.; Zaiss, M.; Chiocca, E.A.; Cohen, O.; Rosen, M.S.; Farrar, C.T. Quantitative imaging of apoptosis following oncolytic virotherapy by magnetic resonance fingerprinting aided by deep learning. *Nat. Biomed. Eng.* **2021**, *1*–10. [[CrossRef](#)]

105. Ross, B.D.; Higgins, R.J.; Boggan, J.E.; Knittel, B.; Garwood, M.  $^{31}\text{P}$  NMR spectroscopy of the in vivo metabolism of an intracerebral glioma in the rat. *Magn. Reson. Med.* **1988**, *6*, 403–417. [CrossRef] [PubMed]
106. Maintz, D.; Heindel, W.; Kugel, H.; Jaeger, R.; Lackner, K.J. Phosphorus-31 MR spectroscopy of normal adult human brain and brain tumours. *NMR Biomed.* **2002**, *15*, 18–27. [CrossRef]
107. Ray, K.J.; Simard, M.A.; Larkin, J.R.; Coates, J.; Kinchesh, P.; Smart, S.C.; Higgins, G.S.; Chappell, M.A.; Sibson, N.R. Tumor pH and Protein Concentration Contribute to the Signal of Amide Proton Transfer Magnetic Resonance Imaging. *Cancer Res.* **2019**, *79*, 1343–1352. [CrossRef] [PubMed]
108. Schure, J.R.; Shrestha, M.; Breuer, S.; Deichmann, R.; Hattingen, E.; Wagner, M.; Pilatus, U. The pH sensitivity of APT-CEST using phosphorus spectroscopy as a reference method. *NMR Biomed.* **2019**, *32*, e4125. [CrossRef]
109. Jeong, H.-K.; Han, K.; Zhou, J.; Zhao, Y.; Choi, Y.S.; Lee, S.-K.; Ahn, S.S. Characterizing amide proton transfer imaging in haemorrhage brain lesions using 3T MRI. *Eur. Radiol.* **2017**, *27*, 1577–1584. [CrossRef]
110. Grossman, R.; Tyler, B.; Brem, H.; Eberhart, C.G.; Wang, S.; Fu, D.-X.; Wen, Z.; Zhou, J. Growth properties of SF188/V+ human glioma in rats in vivo observed by magnetic resonance imaging. *J. Neurooncol.* **2012**, *110*, 315–323. [CrossRef]
111. Kamimura, K.; Nakajo, M.; Yoneyama, T.; Fukukura, Y.; Hirano, H.; Goto, Y.; Sasaki, M.; Akamine, Y.; Keupp, J.; Yoshiura, T. Histogram analysis of amide proton transfer-weighted imaging: Comparison of glioblastoma and solitary brain metastasis in enhancing tumors and peritumoral regions. *Eur. Radiol.* **2019**, *29*, 4133–4140. [CrossRef]
112. Suzuki, H.; Aoki, K.; Chiba, K.; Sato, Y.; Shiozawa, Y.; Shiraishi, Y.; Shimamura, T.; Niida, A.; Motomura, K.; Ohka, F.; et al. Mutational landscape and clonal architecture in grade II and III gliomas. *Nat. Genet.* **2015**, *47*, 458–468. [CrossRef] [PubMed]
113. Olar, A.; Wani, K.M.; Alfaro-Munoz, K.D.; Heathcock, L.E.; van Thuijl, H.F.; Gilbert, M.R.; Armstrong, T.S.; Sulman, E.P.; Cahill, D.P.; Vera-Bolanos, E.; et al. IDH mutation status and role of WHO grade and mitotic index in overall survival in grade II-III diffuse gliomas. *Acta Neuropathol.* **2015**, *129*, 585–596. [CrossRef] [PubMed]
114. Tateishi, K.; Wakimoto, H.; Cahill, D.P. IDH1 Mutation and World Health Organization 2016 Diagnostic Criteria for Adult Diffuse Gliomas: Advances in Surgical Strategy. *Neurosurgery* **2017**, *64*, 134–138. [CrossRef] [PubMed]
115. Cai, K.; Singh, A.; Poptani, H.; Li, W.; Yang, S.; Lu, Y.; Hariharan, H.; Zhou, X.J.; Reddy, R. CEST signal at 2ppm (CEST@2ppm) from Z-spectral fitting correlates with creatine distribution in brain tumor. *NMR Biomed.* **2015**, *28*, 1–8. [CrossRef] [PubMed]
116. Cai, K.; Tain, R.W.; Zhou, X.J.; Damen, F.C.; Scotti, A.M.; Hariharan, H.; Poptani, H.; Reddy, R. Creatine CEST MRI for Differentiating Gliomas with Different Degrees of Aggressiveness. *Mol. Imaging Biol.* **2017**, *19*, 225–232. [CrossRef]
117. Zhang, X.Y.; Wang, F.; Li, H.; Xu, J.; Gochberg, D.F.; Gore, J.C.; Zu, Z. CEST imaging of fast exchanging amine pools with corrections for competing effects at 9.4T. *NMR Biomed.* **2017**, *30*, e3715. [CrossRef]
118. Debnath, A.; Hariharan, H.; Nanga, R.P.R.; Reddy, R.; Singh, A. Glutamate-Weighted CEST Contrast After Removal of Magnetization Transfer Effect in Human Brain and Rat Brain with Tumor. *Mol. Imaging Biol.* **2020**, *22*, 1087–1101. [CrossRef]
119. Heo, H.Y.; Zhang, Y.; Jiang, S.; Lee, D.H.; Zhou, J. Quantitative assessment of amide proton transfer (APT) and nuclear overhauser enhancement (NOE) imaging with extrapolated semisolid magnetization transfer reference (EMR) signals: II. Comparison of three EMR models and application to human brain glioma at 3 Tesla. *Magn. Reson. Med.* **2016**, *75*, 1630–1639. [CrossRef]
120. Sun, H.; Xin, J.; Zhou, J.; Lu, Z.; Guo, Q. Applying Amide Proton Transfer MR Imaging to Hybrid Brain PET/MR: Concordance with Gadolinium Enhancement and Added Value to [(18)F]FDG PET. *Mol. Imaging Biol.* **2018**, *20*, 473–481. [CrossRef]
121. Zaiss, M.; Kunz, P.; Goerke, S.; Radbruch, A.; Bachert, P. MR imaging of protein folding in vitro employing nuclear-Overhauser-mediated saturation transfer. *NMR Biomed.* **2013**, *26*, 1815–1822. [CrossRef]
122. Chan, K.W.; Bulte, J.W.; McMahon, M.T. Diamagnetic chemical exchange saturation transfer (diaCEST) liposomes: Physicochemical properties and imaging applications. *WIREs Nanomed. Nanobiotechnol.* **2013**, *6*, 111–124. [CrossRef] [PubMed]
123. Chen, Z.; Han, Z.; Liu, G. Repurposing Clinical Agents for Chemical Exchange Saturation Transfer Magnetic Resonance Imaging: Current Status and Future Perspectives. *Pharmaceutics* **2020**, *14*, 11. [CrossRef] [PubMed]
124. Ferrauto, G.; Delli Castelli, D.; Di Gregorio, E.; Terreno, E.; Aime, S. LipoCEST and cellCEST imaging agents: Opportunities and challenges. *Wiley Interdiscip. Rev. Nanomed. Nanobiotechnol.* **2016**, *8*, 602–618. [CrossRef] [PubMed]
125. Pagel, M.M. The Pursuit of Theranostics with CEST MRI. *Theranostics* **2016**, *6*, 1601–1602. [CrossRef]
126. Scott, J.N.; Brasher, P.M.A.; Sevick, R.J.; Rewcastle, N.B.; Forsyth, P.A. How often are nonenhancing supratentorial gliomas malignant? A population study. *Neurology* **2002**, *59*, 947. [CrossRef]
127. Cowper, S.E.; Robin, H.S.; Steinberg, S.M.; Su, L.D.; Gupta, S.; LeBoit, P.E. Scleromyxoedema-like cutaneous diseases in renal-dialysis patients. *Lancet* **2000**, *356*, 1000–1001. [CrossRef]
128. FDA. FDA Drug Safety Podcast: FDA Warns That gadolinium-Based Contrast Agents (GBCAs) Are Retained in the Body; Requires New Class Warnings. Available online: <https://www.fda.gov/drugs/fda-drug-safety-podcasts/fda-drug-safety-podcast-fda-warns-gadolinium-based-contrast-agents-gbcas-are-retained-body-requires> (accessed on 26 January 2022).
129. Behzadi, A.H.; Zhao, Y.; Farooq, Z.; Prince, M.R. Immediate allergic reactions to gadolinium-based contrast agents: A systematic review and meta-analysis. *Radiology* **2018**, *286*, 471–482. [CrossRef]
130. Chan, K.; McMahon, M.; Kato, Y.; Liu, G.; Bulte, J.; Bhujwalla, Z.; Artemov, D.; van Zijl, P. Natural D-Glucose as a biodegradable MRI contrast agent for detecting cancer. *Magn. Reson. Med. Off. J. Soc. Magn. Reson. Med. / Soc. Magn. Reson. Med.* **2012**, *68*, 1764–1773. [CrossRef]
131. Nasrallah, F.A.; Pagès, G.; Kuchel, P.W.; Golay, X.; Chuang, K.H. Imaging brain deoxyglucose uptake and metabolism by glucoCEST MRI. *J. Cereb. Blood Flow. Metab.* **2013**, *33*, 1270–1278. [CrossRef]

132. Wang, J.; Weygand, J.; Hwang, K.-P.; Mohamed, A.S.R.; Ding, Y.; Fuller, C.D.; Lai, S.Y.; Frank, S.J.; Zhou, J. Magnetic Resonance Imaging of Glucose Uptake and Metabolism in Patients with Head and Neck Cancer. *Sci. Rep.* **2016**, *6*, 30618. [[CrossRef](#)]
133. Sehgal, A.A.; Li, Y.; Lal, B.; Yadav, N.N.; Xu, X.; Xu, J.; Laterra, J.; van Zijl, P.C.M. CEST MRI of 3-O-methyl-D-glucose uptake and accumulation in brain tumors. *Magn. Reson. Med.* **2019**, *81*, 1993–2000. [[CrossRef](#)] [[PubMed](#)]
134. Rivlin, M.; Horev, J.; Tsarfaty, I.; Navon, G. Molecular imaging of tumors and metastases using chemical exchange saturation transfer (CEST) MRI. *Sci. Rep.* **2013**, *3*, 3045. [[CrossRef](#)] [[PubMed](#)]
135. Walker-Samuel, S.; Ramasawmy, R.; Torrealdea, F.; Rega, M.; Rajkumar, V.; Johnson, S.P.; Richardson, S.; Gonçalves, M.; Parkes, H.G.; Arstad, E.; et al. In vivo imaging of glucose uptake and metabolism in tumors. *Nat. Med.* **2013**, *19*, 1067–1072. [[CrossRef](#)] [[PubMed](#)]
136. Xu, X.; Xu, J.; Knutsson, L.; Liu, J.; Liu, H.; Li, Y.; Lal, B.; Laterra, J.; Artemov, D.; Liu, G.; et al. The effect of the mTOR inhibitor rapamycin on glucoCEST signal in a preclinical model of glioblastoma. *Magn. Reson. Med.* **2019**, *81*, 3798–3807. [[CrossRef](#)] [[PubMed](#)]
137. Huang, J.; Lai, J.H.; Han, X.; Chen, Z.; Xiao, P.; Liu, Y.; Chen, L.; Xu, J.; Chan, K.W. Sensitivity schemes for dynamic glucose-enhanced magnetic resonance imaging to detect glucose uptake and clearance in mouse brain at 3 T. *NMR Biomed.* **2022**, *35*, e4640. [[CrossRef](#)]
138. Huang, J.; van Zijl, P.C.; Han, X.; Dong, C.M.; Cheng, G.W.; Tse, K.-H.; Knutsson, L.; Chen, L.; Lai, J.H.; Wu, E.X. Altered d-glucose in brain parenchyma and cerebrospinal fluid of early Alzheimer’s disease detected by dynamic glucose-enhanced MRI. *Sci. Adv.* **2020**, *6*, eaba3884. [[CrossRef](#)]
139. Xu, X.; Chan, K.W.; Knutsson, L.; Artemov, D.; Xu, J.; Liu, G.; Kato, Y.; Lal, B.; Laterra, J.; McMahon, M.T.; et al. Dynamic glucose enhanced (DGE) MRI for combined imaging of blood-brain barrier break down and increased blood volume in brain cancer. *Magn. Reson. Med.* **2015**, *74*, 1556–1563. [[CrossRef](#)]
140. Xu, X.; Yadav, N.N.; Knutsson, L.; Hua, J.; Kalyani, R.; Hall, E.; Laterra, J.; Blakeley, J.; Strowd, R.; Pomper, M.; et al. Dynamic Glucose-Enhanced (DGE) MRI: Translation to Human Scanning and First Results in Glioma Patients. *Tomography* **2015**, *1*, 105–114. [[CrossRef](#)]
141. Herz, K.; Lindig, T.; Deshmame, A.; Schittenhelm, J.; Skardelly, M.; Bender, B.; Ernemann, U.; Scheffler, K.; Zaiss, M. T1ρ-based dynamic glucose-enhanced (DGEρ) MRI at 3 T: Method development and early clinical experience in the human brain. *Magn. Reson. Med.* **2019**, *82*, 1832–1847. [[CrossRef](#)]
142. Xu, X.; Sehgal, A.A.; Yadav, N.N.; Laterra, J.; Blair, L.; Blakeley, J.; Seidemo, A.; Coughlin, J.M.; Pomper, M.G.; Knutsson, L.; et al. d-glucose weighted chemical exchange saturation transfer (glucoCEST)-based dynamic glucose enhanced (DGE) MRI at 3T: Early experience in healthy volunteers and brain tumor patients. *Magn. Reson. Med.* **2020**, *84*, 247–262. [[CrossRef](#)]
143. Zu, Z.; Spear, J.; Li, H.; Xu, J.; Gore, J.C. Measurement of regional cerebral glucose uptake by magnetic resonance spin-lock imaging. *Magn. Reson. Imaging* **2014**, *32*, 1078–1084. [[CrossRef](#)]
144. Jin, T.; Iordanova, B.; Hitchens, T.K.; Modo, M.; Wang, P.; Mehren, H.; Kim, S.G. Chemical exchange-sensitive spin-lock (CESL) MRI of glucose and analogs in brain tumors. *Magn. Reson. Med.* **2018**, *80*, 488–495. [[CrossRef](#)] [[PubMed](#)]
145. Zu, Z.; Jiang, X.; Xu, J.; Gore, J.C. Spin-lock imaging of 3-o-methyl-D glucose (3oMG) in brain tumors. *Magn. Reson. Med.* **2018**, *80*, 1110–1117. [[CrossRef](#)]
146. Haris, M.; Singh, A.; Mohammed, I.; Ittyerah, R.; Nath, K.; Nanga, R.P.R.; Debrosse, C.; Kogan, F.; Cai, K.; Poptani, H.; et al. In vivo magnetic resonance imaging of tumor protease activity. *Sci. Rep.* **2014**, *4*, 6081. [[CrossRef](#)] [[PubMed](#)]
147. Li, Y.; Chen, H.; Xu, J.; Yadav, N.N.; Chan, K.W.Y.; Luo, L.; McMahon, M.T.; Vogelstein, B.; van Zijl, P.C.M.; Zhou, S.; et al. CEST theranostics: Label-free MR imaging of anticancer drugs. *Oncotarget* **2016**, *7*, 6369–6378. [[CrossRef](#)] [[PubMed](#)]
148. Barenholz, Y. Doxil(R)—The first FDA-approved nano-drug: Lessons learned. *J. Control. Release Off. J. Control. Release Soc.* **2012**, *160*, 117–134. [[CrossRef](#)] [[PubMed](#)]
149. Liu, G.; Moake, M.; Har-el, Y.E.; Long, C.M.; Chan, K.W.; Cardona, A.; Jamil, M.; Walczak, P.; Gilad, A.A.; Sgouros, G.; et al. In vivo multicolor molecular MR imaging using diamagnetic chemical exchange saturation transfer liposomes. *Magn. Reson. Med.* **2012**, *67*, 1106–1113. [[CrossRef](#)]
150. Zhao, J.M.; Har-el, Y.E.; McMahon, M.T.; Zhou, J.; Sherry, A.D.; Sgouros, G.; Bulte, J.W.; van Zijl, P.C. Size-induced enhancement of chemical exchange saturation transfer (CEST) contrast in liposomes. *J. Am. Chem. Soc.* **2008**, *130*, 5178–5184. [[CrossRef](#)]
151. Terreno, E.; Castelli, D.D.; Milone, L.; Rollet, S.; Stancanello, J.; Violante, E.; Aime, S. First ex-vivo MRI co-localization of two LIPOCEST agents. *Contrast. Media Mol. Imaging* **2008**, *3*, 38–43. [[CrossRef](#)]
152. Chen, Z.; Li, Y.; Airan, R.; Han, Z.; Xu, J.; Chan, K.W.Y.; Xu, Y.; Bulte, J.W.M.; van Zijl, P.C.M.; McMahon, M.T.; et al. CT and CEST MRI bimodal imaging of the intratumoral distribution of iodinated liposomes. *Quant. Imaging Med. Surg.* **2019**, *9*, 1579–1591. [[CrossRef](#)]
153. Chan, K.W.; Yu, T.; Qiao, Y.; Liu, Q.; Yang, M.; Patel, H.; Liu, G.; Kinzler, K.W.; Vogelstein, B.; Bulte, J.W.; et al. A diaCEST MRI approach for monitoring liposomal accumulation in tumors. *J. Control Release* **2014**, *180*, 51–59. [[CrossRef](#)] [[PubMed](#)]
154. Yang, M.; Yu, T.; Wang, Y.Y.; Lai, S.K.; Zeng, Q.; Miao, B.; Tang, B.C.; Simons, B.W.; Ensign, L.M.; Liu, G.; et al. Vaginal Delivery of Paclitaxel via Nanoparticles with Non-Mucoadhesive Surfaces Suppresses Cervical Tumor Growth. *Adv Healthc Mater* **2013**, *3*, 1044–1052. [[CrossRef](#)]

155. Yu, T.; Chan, K.W.; Anonuevo, A.; Song, X.; Schuster, B.S.; Chattopadhyay, S.; Xu, Q.; Oskolkov, N.; Patel, H.; Ensign, L.M.; et al. Liposome-based mucus-penetrating particles (MPP) for mucosal theranostics: Demonstration of diamagnetic chemical exchange saturation transfer (diaCEST) magnetic resonance imaging (MRI). *Nanomed. Nanotechnol. Biol. Med.* **2015**, *11*, 401–405. [CrossRef] [PubMed]
156. Law, L.H.; Xiao, P.; Huang, J.; HAN, X.; Chan, K.W. CEST Imaging of Nose-to-Brain Drug Delivery using Iohexol liposomes at 3T. In Proceedings of the ISMRM & SMRT Annual Meeting & Exhibition, Online, 15–20 May 2021. No. 0720.
157. Yuan, Y.; Zhang, J.; Qi, X.; Li, S.; Liu, G.; Siddhanta, S.; Barman, I.; Song, X.; McMahon, M.T.; Bulte, J.W.M. Furin-mediated intracellular self-assembly of olsalazine nanoparticles for enhanced magnetic resonance imaging and tumour therapy. *Nat. Mater.* **2019**, *18*, 1376–1383. [CrossRef] [PubMed]
158. Chan, K.W.Y.; Liu, G.; Song, X.; Kim, H.; Yu, T.; Arifin, D.R.; Gilad, A.A.; Hanes, J.; Walczak, P.; van Zijl, P.C.M.; et al. MRI-detectable pH nanosensors incorporated into hydrogels for in vivo sensing of transplanted-cell viability. *Nat. Mater.* **2013**, *12*, 268–275. [CrossRef] [PubMed]
159. Lock, L.L.; Li, Y.; Mao, X.; Chen, H.; Staedtke, V.; Bai, R.; Ma, W.; Lin, R.; Li, Y.; Liu, G.; et al. One-Component Supramolecular Filament Hydrogels as Theranostic Label-Free Magnetic Resonance Imaging Agents. *ACS Nano* **2017**, *11*, 797–805. [CrossRef] [PubMed]
160. Venur, V.A.; Peereboom, D.M.; Ahluwalia, M.S. Current medical treatment of glioblastoma. *Cancer Treat. Res.* **2015**, *163*, 103–115. [CrossRef]
161. Bregy, A.; Shah, A.H.; Diaz, M.V.; Pierce, H.E.; Ames, P.L.; Diaz, D.; Komotor, R.J. The role of Gliadel wafers in the treatment of high-grade gliomas. *Expert. Rev. Anticancer Ther.* **2013**, *13*, 1453–1461. [CrossRef]
162. Tyler, B.; Fowers, K.D.; Li, K.W.; Recinos, V.R.; Caplan, J.M.; Hdeib, A.; Grossman, R.; Basaldella, L.; Bekelis, K.; Pradilla, G.; et al. A thermal gel depot for local delivery of paclitaxel to treat experimental brain tumors in rats. *J. Neurosurg.* **2010**, *113*, 210–217. [CrossRef]
163. Kim, J.I.; Kim, B.; Chun, C.; Lee, S.H.; Song, S.-C. MRI-monitored long-term therapeutic hydrogel system for brain tumors without surgical resection. *Biomaterials* **2012**, *33*, 4836–4842. [CrossRef]
164. Bastianich, C.; Vanvarenberg, K.; Ucakar, B.; Pitorre, M.; Bastiat, G.; Lagarce, F.; Préat, V.; Danhier, F. Lauroyl-gemcitabine-loaded lipid nanocapsule hydrogel for the treatment of glioblastoma. *J. Control. Release* **2016**, *225*, 283–293. [CrossRef]
165. Vellimana, A.K.; Recinos, V.R.; Hwang, L.; Fowers, K.D.; Li, K.W.; Zhang, Y.; Okonma, S.; Eberhart, C.G.; Brem, H.; Tyler, B.M. Combination of paclitaxel thermal gel depot with temozolomide and radiotherapy significantly prolongs survival in an experimental rodent glioma model. *J. Neuro-Oncol.* **2013**, *111*, 229–236. [CrossRef] [PubMed]
166. Han, X.; Huang, J.; To, A.K.W.; Lai, J.H.C.; Xiao, P.; Wu, E.X.; Xu, J.; Chan, K.W.Y. CEST MRI detectable liposomal hydrogels for multiparametric monitoring in the brain at 3T. *Theranostics* **2020**, *10*, 2215–2228. [CrossRef]
167. Han, X.; Lai, J.H.C.; Huang, J.; Park, S.W.; Liu, Y.; Chan, K.W.Y. Imaging Self-Healing Hydrogels and Chemotherapeutics Using CEST MRI at 3 T. *ACS Appl. Bio Mater.* **2021**, *4*, 5605–5616. [CrossRef] [PubMed]
168. Zhang, X.Y.; Zhai, Y.; Jin, Z.; Li, C.; Sun, P.Z.; Wu, Y. Preliminary demonstration of in vivo quasi-steady-state CEST postprocessing—Correction of saturation time and relaxation delay for robust quantification of tumor MT and APT effects. *Magn. Reson. Med.* **2021**, *86*, 943–953. [CrossRef] [PubMed]
169. van Zijl, P.C.M.; Lam, W.W.; Xu, J.; Knutsson, L.; Stanisz, G.J. Magnetization Transfer Contrast and Chemical Exchange Saturation Transfer MRI. Features and analysis of the field-dependent saturation spectrum. *Neuro Image* **2018**, *168*, 222–241. [CrossRef] [PubMed]
170. Bryant, R.G. The dynamics of water-protein interactions. *Annu. Rev. Biophys. Biomol. Struct.* **1996**, *25*, 29–53. [CrossRef]
171. Poblador Rodriguez, E.; Moser, P.; Dymerska, B.; Robinson, S.; Schmitt, B.; van der Kouwe, A.; Gruber, S.; Trattnig, S.; Bogner, W. A comparison of static and dynamic  $\Delta B_0$  mapping methods for correction of CEST MRI in the presence of temporal B0 field variations. *Magn. Reson. Med.* **2019**, *82*, 633–646. [CrossRef]
172. Stancanello, J.; Terreno, E.; Castelli, D.D.; Cabella, C.; Uggeri, F.; Aime, S. Development and validation of a smoothing-splines-based correction method for improving the analysis of CEST-MR images. *Contrast Media Mol. Imaging* **2008**, *3*, 136–149. [CrossRef]
173. Kim, M.; Gillen, J.; Landman, B.A.; Zhou, J.; Van Zijl, P.C. Water saturation shift referencing (WASSR) for chemical exchange saturation transfer (CEST) experiments. *Magn. Reson. Med. Off. J. Int. Soc. Magn. Reson. Med.* **2009**, *61*, 1441–1450. [CrossRef]
174. Sun, P.Z.; Farrar, C.T.; Sorensen, A.G. Correction for artifacts induced by B0 and B1 field inhomogeneities in pH-sensitive chemical exchange saturation transfer (CEST) imaging. *Magn. Reson. Med. Off. J. Int. Soc. Magn. Reson. Med.* **2007**, *58*, 1207–1215. [CrossRef]
175. Sui, R.; Chen, L.; Li, Y.; Huang, J.; Chan, K.W.; Xu, X.; van Zijl, P.C.; Xu, J. Whole-brain amide CEST imaging at 3T with a steady-state radial MRI acquisition. *Magn. Reson. Med.* **2021**, *86*, 893–906. [CrossRef]
176. Schuenke, P.; Windschuh, J.; Roeloffs, V.; Ladd, M.E.; Bachert, P.; Zaiss, M. Simultaneous mapping of water shift and B1 (WASABI)—Application to field-inhomogeneity correction of CEST MRI data. *Magn. Reson. Med.* **2017**, *77*, 571–580. [CrossRef]
177. Khlebnikov, V.; Windschuh, J.; Siero, J.C.; Zaiss, M.; Luijten, P.R.; Klomp, D.W.; Hoogduin, H. On the transmit field inhomogeneity correction of relaxation-compensated amide and NOE CEST effects at 7 T. *NMR Biomed.* **2017**, *30*, e3687. [CrossRef]
178. Sun, P.Z.; Benner, T.; Kumar, A.; Sorensen, A.G. Investigation of optimizing and translating pH-sensitive pulsed-chemical exchange saturation transfer (CEST) imaging to a 3T clinical scanner. *Magn. Reson. Med. Off. J. Int. Soc. Magn. Reson. Med.* **2008**, *60*, 834–841. [CrossRef]

179. Jones, C.K.; Polders, D.; Hua, J.; Zhu, H.; Hoogduin, H.J.; Zhou, J.; Luijten, P.; van Zijl, P.C. In vivo three-dimensional whole-brain pulsed steady-state chemical exchange saturation transfer at 7 T. *Magn. Reson. Med.* **2012**, *67*, 1579–1589. [\[CrossRef\]](#)
180. Zaiss, M.; Schmitt, B.; Bachert, P. Quantitative separation of CEST effect from magnetization transfer and spillover effects by Lorentzian-line-fit analysis of z-spectra. *J. Magn. Reson.* **2011**, *211*, 149–155. [\[CrossRef\]](#)
181. Zhou, I.Y.; Wang, E.; Cheung, J.S.; Zhang, X.; Fulci, G.; Sun, P.Z. Quantitative chemical exchange saturation transfer (CEST) MRI of glioma using Image Downsampling Expedited Adaptive Least-squares (IDEAL) fitting. *Sci. Rep.* **2017**, *7*, 1–10. [\[CrossRef\]](#)
182. Chen, L.; Barker, P.B.; Weiss, R.G.; van Zijl, P.C.; Xu, J. Creatine and phosphocreatine mapping of mouse skeletal muscle by a polynomial and Lorentzian line-shape fitting CEST method. *Magn. Reson. Med.* **2019**, *81*, 69–78. [\[CrossRef\]](#)
183. Chen, L.; Wei, Z.; Cai, S.; Li, Y.; Liu, G.; Lu, H.; Weiss, R.G.; van Zijl, P.C.; Xu, J. High-resolution creatine mapping of mouse brain at 11.7 T using non-steady-state chemical exchange saturation transfer. *NMR Biomed.* **2019**, *32*, e4168. [\[CrossRef\]](#)
184. Chen, L.; Zeng, H.; Xu, X.; Yadav, N.N.; Cai, S.; Puts, N.A.; Barker, P.B.; Li, T.; Weiss, R.G.; van Zijl, P.C. Investigation of the contribution of total creatine to the CEST Z-spectrum of brain using a knockout mouse model. *NMR Biomed.* **2017**, *30*, e3834. [\[CrossRef\]](#)
185. Jin, T.; Wang, P.; Zong, X.; Kim, S.G. MR imaging of the amide-proton transfer effect and the pH-insensitive nuclear Overhauser effect at 9.4 T. *Magn. Reson. Med.* **2013**, *69*, 760–770. [\[CrossRef\]](#)
186. Sun, P.Z.; Benner, T.; Copen, W.A.; Sorensen, A.G. Early experience of translating pH-weighted MRI to image human subjects at 3 Tesla. *Stroke* **2010**, *41*, S147–S151. [\[CrossRef\]](#)
187. Zhang, X.Y.; Wang, F.; Li, H.; Xu, J.; Gochberg, D.F.; Gore, J.C.; Zu, Z. Accuracy in the quantification of chemical exchange saturation transfer (CEST) and relayed nuclear Overhauser enhancement (rNOE) saturation transfer effects. *NMR Biomed.* **2017**, *30*, e3716. [\[CrossRef\]](#)
188. Huang, J.; Lai, J.H.; Tse, K.-H.; Cheng, G.W.; Liu, Y.; Chen, Z.; Han, X.; Chen, L.; Xu, J.; Chan, K.W. Deep neural network based CEST and AREX processing: Application in imaging a model of Alzheimer's disease at 3 T. *Magn. Reson. Med.* **2022**, *87*, 1529–1545. [\[CrossRef\]](#)
189. Zaiss, M.; Xu, J.; Goerke, S.; Khan, I.S.; Singer, R.J.; Gore, J.C.; Gochberg, D.F.; Bachert, P. Inverse Z-spectrum analysis for spillover-, MT-, and T1-corrected steady-state pulsed CEST-MRI—application to pH-weighted MRI of acute stroke. *NMR Biomed.* **2014**, *27*, 240–252. [\[CrossRef\]](#)
190. Cohen, O.; Huang, S.; McMahon, M.T.; Rosen, M.S.; Farrar, C.T. Rapid and quantitative chemical exchange saturation transfer (CEST) imaging with magnetic resonance fingerprinting (MRF). *Magn. Reson. Med.* **2018**, *80*, 2449–2463. [\[CrossRef\]](#)
191. Kim, B.; Schär, M.; Park, H.; Heo, H.-Y. A deep learning approach for magnetization transfer contrast MR fingerprinting and chemical exchange saturation transfer imaging. *Neuro Image* **2020**, *221*, 117165. [\[CrossRef\]](#)
192. LeCun, Y.; Bengio, Y.; Hinton, G. Deep learning. *Nature* **2015**, *521*, 436–444. [\[CrossRef\]](#)
193. Kang, B.; Kim, B.; Schär, M.; Park, H.; Heo, H.Y. Unsupervised learning for magnetization transfer contrast MR fingerprinting: Application to CEST and nuclear Overhauser enhancement imaging. *Magn. Reson. Med.* **2021**, *85*, 2040–2054. [\[CrossRef\]](#)
194. Svolos, P.; Kousi, E.; Kapsalaki, E.; Theodorou, K.; Fezoulidis, I.; Kappas, C.; Tsougos, I. The role of diffusion and perfusion weighted imaging in the differential diagnosis of cerebral tumors: A review and future perspectives. *Cancer Imaging* **2014**, *14*, 1–20. [\[CrossRef\]](#)
195. Field, A.S.; Alexander, A.L.; Wu, Y.C.; Hasan, K.M.; Witwer, B.; Badie, B. Diffusion tensor eigenvector directional color imaging patterns in the evaluation of cerebral white matter tracts altered by tumor. *J. Magn. Reson. Imaging Off. J. Int. Soc. Magn. Reson. Med.* **2004**, *20*, 555–562. [\[CrossRef\]](#)
196. Dangouloff-Ros, V.; Deroulers, C.; Foissac, F.; Badoual, M.; Shotar, E.; Grévent, D.; Calmon, R.; Pages, M.; Grill, J.; Dufour, C. Arterial spin labeling to predict brain tumor grading in children: Correlations between histopathologic vascular density and perfusion MR imaging. *Radiology* **2016**, *281*, 553–566. [\[CrossRef\]](#)
197. Warmuth, C.; Gunther, M.; Zimmer, C. Quantification of blood flow in brain tumors: Comparison of arterial spin labeling and dynamic susceptibility-weighted contrast-enhanced MR imaging. *Radiology* **2003**, *228*, 523–532. [\[CrossRef\]](#)
198. Heye, A.K.; Culling, R.D.; Hernández, M.d.C.V.; Thrippleton, M.J.; Wardlaw, J.M. Assessment of blood–brain barrier disruption using dynamic contrast-enhanced MRI. A systematic review. *Neuro Image Clin.* **2014**, *6*, 262–274. [\[CrossRef\]](#)
199. Shiroishi, M.S.; Castellazzi, G.; Boxerman, J.L.; D'Amore, F.; Essig, M.; Nguyen, T.B.; Provenzale, J.M.; Enterline, D.S.; Anzalone, N.; Dörfler, A. Principles of T2\*-weighted dynamic susceptibility contrast MRI technique in brain tumor imaging. *J. Magn. Reson. Imaging* **2015**, *41*, 296–313. [\[CrossRef\]](#)
200. Law, M.; Yang, S.; Babb, J.S.; Knopp, E.A.; Golfinos, J.G.; Zagzag, D.; Johnson, G. Comparison of cerebral blood volume and vascular permeability from dynamic susceptibility contrast-enhanced perfusion MR imaging with glioma grade. *Am. J. Neuroradiol.* **2004**, *25*, 746–755.
201. Wainwright, D.A.; Nigam, P.; Thaci, B.; Dey, M.; Lesniak, M.S. Recent developments on immunotherapy for brain cancer. *Expert Opin. Emerg. Drugs* **2012**, *17*, 181–202. [\[CrossRef\]](#)
202. Ishimaru, H.; Morikawa, M.; Iwanaga, S.; Kaminogo, M.; Ochi, M.; Hayashi, K. Differentiation between high-grade glioma and metastatic brain tumor using single-voxel proton MR spectroscopy. *Eur. Radiol.* **2001**, *11*, 1784–1791. [\[CrossRef\]](#)
203. Ott, D.; Hennig, J.; Ernst, T. Human brain tumors: Assessment with in vivo proton MR spectroscopy. *Radiology* **1993**, *186*, 745–752. [\[CrossRef\]](#)

204. Dunet, V.; Pomoni, A.; Hottinger, A.; Nicod-Lalonde, M.; Prior, J.O. Performance of 18F-FET versus 18F-FDG-PET for the diagnosis and grading of brain tumors: Systematic review and meta-analysis. *Neuro-oncology* **2015**, *18*, 426–434. [[CrossRef](#)]
205. Chao, S.T.; Suh, J.H.; Raja, S.; Lee, S.Y.; Barnett, G. The sensitivity and specificity of FDG PET in distinguishing recurrent brain tumor from radionecrosis in patients treated with stereotactic radiosurgery. *Int. J. Cancer* **2001**, *96*, 191–197. [[CrossRef](#)]
206. Herz, K.; Mueller, S.; Perlman, O.; Zaitsev, M.; Knutsson, L.; Sun, P.Z.; Zhou, J.; van Zijl, P.; Heinecke, K.; Schuenke, P. Pulseq-CEST: Towards multi-site multi-vendor compatibility and reproducibility of CEST experiments using an open-source sequence standard. *Magn. Reson. Med.* **2021**, *86*, 1845–1858. [[CrossRef](#)]
207. Liu, R.; Zhang, H.; Niu, W.; Lai, C.; Ding, Q.; Chen, W.; Liang, S.; Zhou, J.; Wu, D.; Zhang, Y. Improved chemical exchange saturation transfer imaging with real-time frequency drift correction. *Magn. Reson. Med.* **2019**, *81*, 2915–2923. [[CrossRef](#)]
208. Mueller, S.; Stirnberg, R.; Akbey, S.; Ehses, P.; Scheffler, K.; Stöcker, T.; Zaiss, M. Whole brain snapshot CEST at 3T using 3D-EPI: Aiming for speed, volume, and homogeneity. *Magn. Reson. Med.* **2020**, *84*, 2469–2483. [[CrossRef](#)]
209. Villano, D.; Romdhane, F.; Irrera, P.; Consolino, L.; Anemone, A.; Zaiss, M.; Dastrù, W.; Longo, D.L. A fast multislice sequence for 3D MRI-CEST pH imaging. *Magn. Reson. Med.* **2021**, *85*, 1335–1349. [[CrossRef](#)]
210. Zaiss, M.; Ehses, P.; Scheffler, K. Snapshot-CEST: Optimizing spiral-centric-reordered gradient echo acquisition for fast and robust 3D CEST MRI at 9.4 T. *NMR Biomed.* **2018**, *31*, e3879. [[CrossRef](#)]